Precambrian Research 328 (2019) 235–249

Contents lists available at ScienceDirect

Precambrian Research

journal homepage: www.elsevier.com/locate/precamres

Neoproterozoic I-type and highly fractionated A-type granites in the Yili Block, Central Asian Orogenic Belt: Petrogenesis and tectonic implications

Fuhao Xiong[a,b], Mingcai Hou[a,c,*], Peter A. Cawood[d], Hu Huang[a,*], Mihai N. Ducea[e,f], Shijun Ni[b]

[a] State Key Laboratory of Oil and Gas Reservoir Geology and Exploitation, Chengdu University of Technology, Chengdu 610059, China
[b] College of Earth Science, Chengdu University of Technology, Chengdu 610059, China
[c] Institute of Sedimentary Geology, Chengdu University of Technology, Chengdu 610059, China
[d] School of Earth, Atmosphere & Environment, Monash University, Melbourne, VIC 3800, Australia
[e] Department of Geosciences, University of Arizona, Tucson, AZ 85721, USA
[f] Faculty of Geology and Geophysics, University of Bucharest, Bucharest 010041, Romania

ARTICLE INFO

Keywords:
Neoproterozoic
Granites
Petrogenesis
Precambrian evolution
Yili Block

ABSTRACT

The Yili Block in NW China and NE Kazakhstan is a continental fragment within the Central Asian Orogenic Belt (CAOB). We present a systematic study of whole-rock geochemistry, Sr–Nd–Hf isotopic compositions, and U–Pb geochronology of newly identified Neoproterozoic granitic plutons from the southern Yili Block to further constrain the Proterozoic evolution of microcontinents constituting the CAOB. Gneissic, augen, and mylonitized granites yield intrusion $^{206}Pb/^{238}U$ ages of 947 ± 4 Ma, 889 ± 5 Ma, and 892 ± 5 Ma, respectively. The gneissic granites display affinities to calc-alkaline, weakly peraluminous, magnesian I-type granites ($Mg^{\#}$ = 33–34; FeO^T/MgO = 3.49–3.59). The augen and mylonitized granites lie on the ferroan, calc-alkaline, highly fractionated A-type granite trend ($Mg^{\#}$ = 11–21, FeO^T/MgO = 6.52–14.58, SiO_2 > 74 wt%, 10000*Ga/Al = 2.80–3.26). The markedly enriched Sr–Nd–Hf isotopic compositions of the ca. 947 Ma magnesian I-type granites suggest a derivation from ca. 2.0 Ga MgO-rich basement rocks. The varied initial $^{87}Sr/^{86}Sr$ ratios (0.716530–0.720543), chondrite-like εHf(t) values (−2.11 to 0.72), and differentiated incompatible elements of the ca. 890 Ma A-type granites suggest a derivation from partial melting of ca. 1.8 Ga crustal sources, followed by strong fractional crystallization. The Yili Block probably constituted part of an exterior orogen that developed along the margin of the Rodinia supercontinent during the early Neoproterozoic, undergoing a tectonic transition from syn-collisional to post-collisional extension at ca. 890 Ma. This study reveals that crustal reworking played a key role in Neoproterozoic crustal evolution in the Yili Block and that this block has a tectonic affinity to the Central Tianshan Block but is distinct from the Tarim Craton.

1. Introduction

Orogenic belts are the principal sites of growth and recycling of continental crust and provide excellent natural laboratories in which to study linkages between magmatism and tectonic processes (Cawood et al., 2009; DeCelles et al., 2009). The Central Asian Orogenic Belt (CAOB), one of the largest and most complex accretionary orogens on Earth, has been extensively studied to constrain its accretionary history (Kröner et al., 2007; Glorie et al., 2011; Long et al., 2011; Wang et al., 2017; He et al., 2018a). Some of the component blocks of the CAOB record a late Mesoproterozoic to early Neoproterozoic evolution that overlaps with the assembly and break-up of the Rodinia supercontinent (Zhang et al., 2012a; Gao et al., 2015; Degtyarev et al., 2017; Huang et al., 2017).

However, details of the Precambrian evolution of the CAOB remain unclear, particularly concerning the relationship of its Neoproterozoic tectonic evolution to the Rodinia supercontinent (Lu et al., 2008; Zhang et al., 2009, 2012b; Ge et al., 2014a; Wang et al., 2015a,b; Tang et al., 2016; Chen et al., 2017; Wu et al., 2018). Neoproterozoic magmatism occurred in several Precambrian microcontinents constituting the present southwestern CAOB and in the adjacent Tarim Craton (Fig. 1). Understanding the age and geochemical affinities of this magmatic activity is crucial to constraining the evolution of Rodinia. In contrast to the extensive studies of a number of Precambrian blocks in the CAOB (e.g., Cai et al., 2018, and references therein), the Neoproterozoic magmatism of the Yili Block (or the Kazakhstan–Yili block of Zhou et al., 2018) has received little research attention, which limits understanding of the Precambrian evolution of this block. The few studies

* Corresponding authors.
E-mail addresses: houmc@cdut.edu.cn (M. Hou), 118huanghu@163.com (H. Huang).

https://doi.org/10.1016/j.precamres.2019.04.017
Received 27 November 2018; Received in revised form 15 April 2019; Accepted 18 April 2019
Available online 20 April 2019
0301-9268/

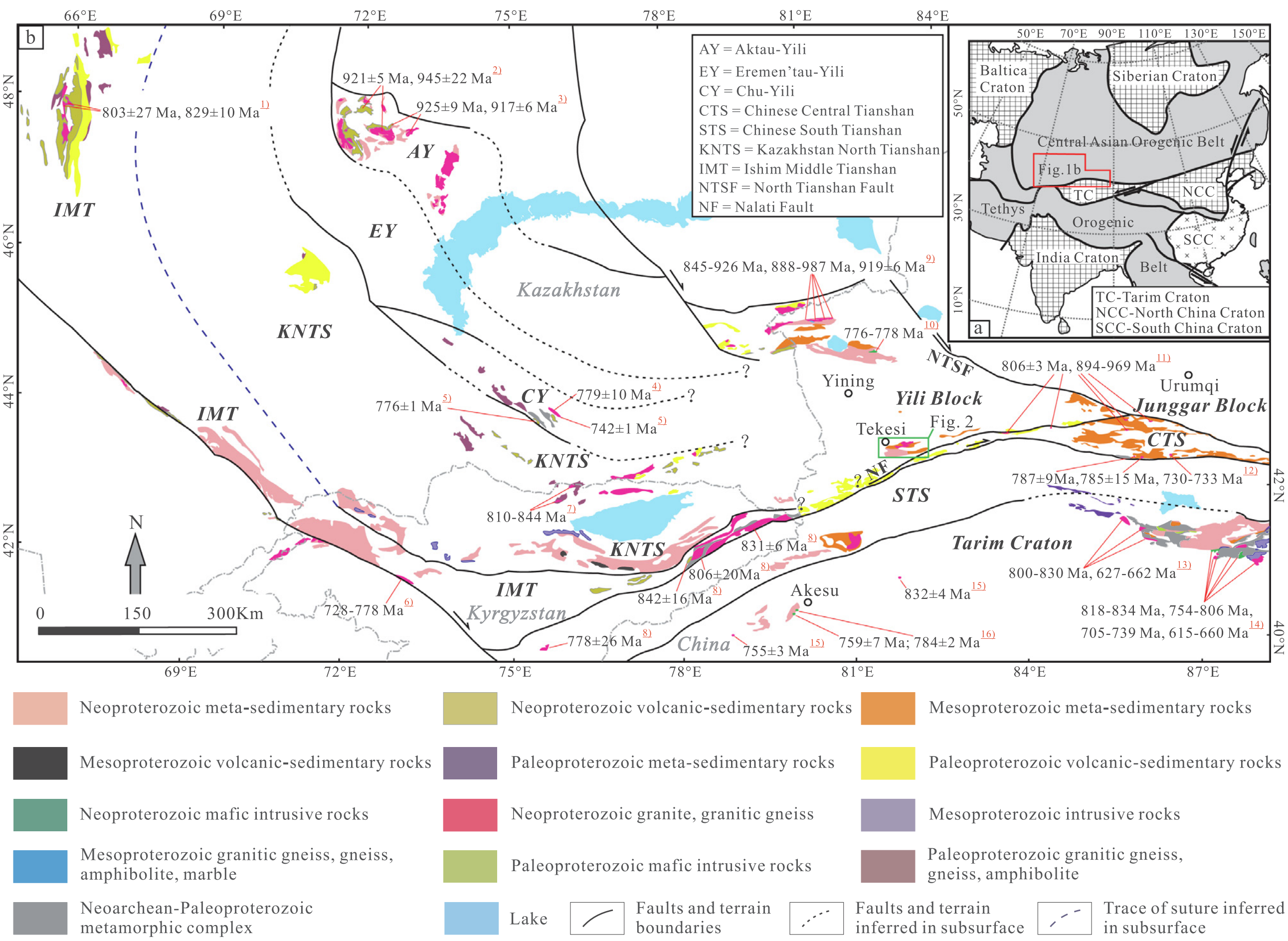

Fig. 1. (a) Simplified tectonic divisions of eastern Eurasia, showing the location of the Central Asian Orogenic Belt (COAB) (modified after Kröner et al. (2007)); (b) Generalized tectonic framework of the southwestern CAOB and major surrounding units (simplified after Levashova et al. (2011)). Data sources: (1) Tretyakov et al. (2011, 2017); (2) Tretyakov et al. (2015); (3) Degtyarev et al. (2008); (4) Pilitsyna et al. (2019); (5) Kröner et al. (2007); (6) Konopelko et al. (2013); (7) Kröner et al. (2012); (8) Glorie et al. (2011); (9) Hu et al. (2010), Wang et al. (2014a), Huang (2017); (10) Wang et al. (2014b); (11) Yang et al. (2008), Long et al. (2011), Gao et al. (2015), Huang et al. (2015b); (12) Wang et al. (2014c, 2017), Gao et al. (2015); (13) Ge et al. (2012, 2013), Zhang et al. (2013 and references therein); (14) Chen et al. (2017), Han et al. (2018 and references therein); (15) Xu et al. (2013); (16) Zhang et al. (2009, 2012a).

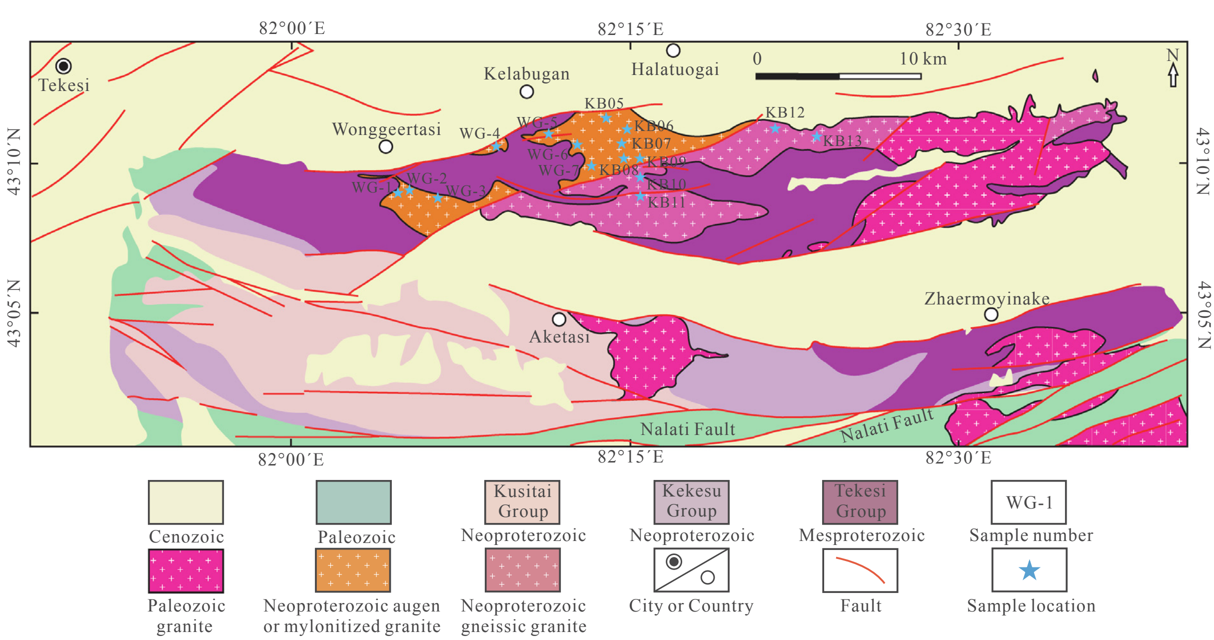

Fig. 2. Simplified geological map with sampling locations of the studied Neoproterozoic granites in the southern Yili Block (modified after XBGMR, 1978).

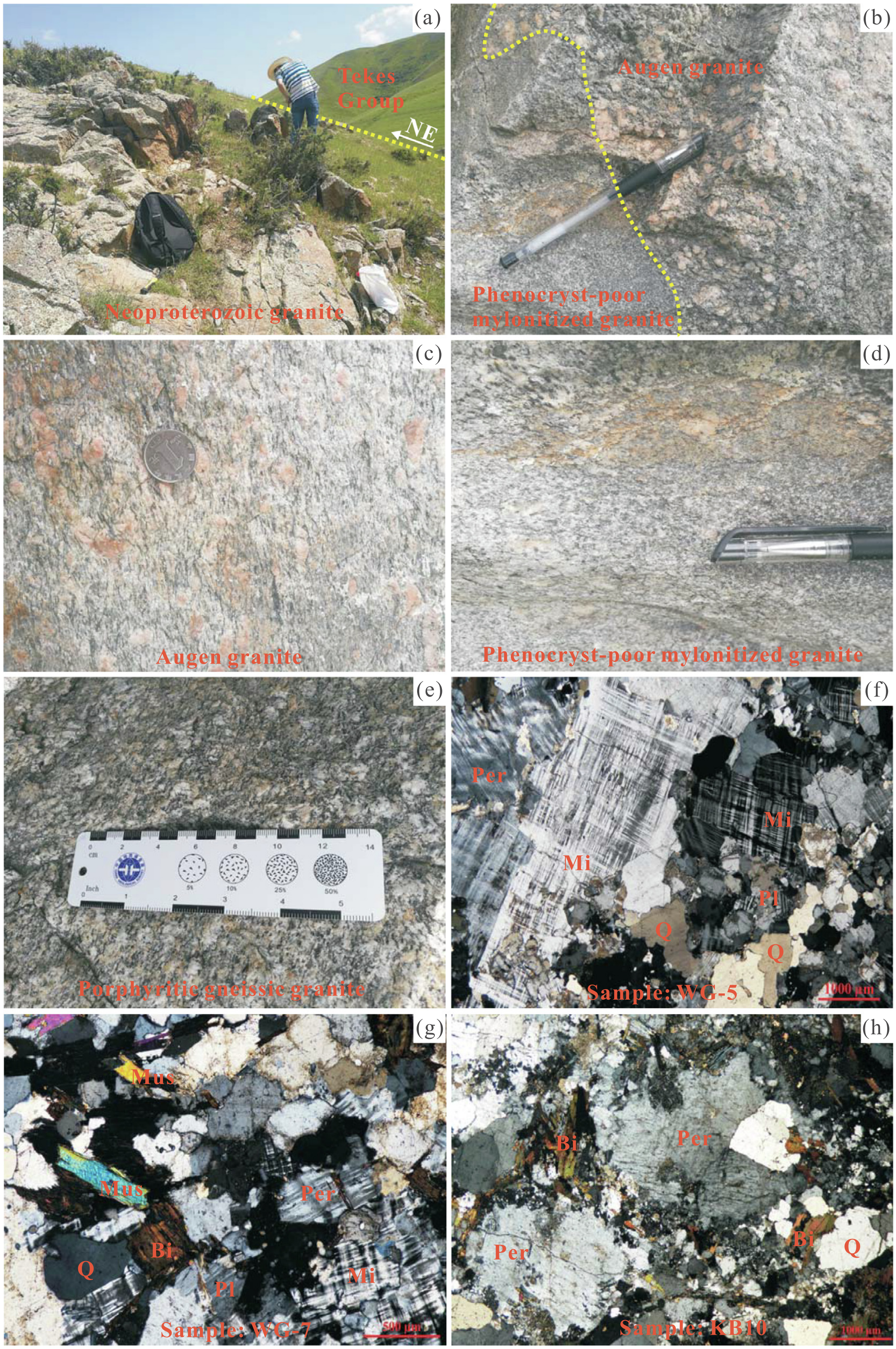

Fig. 3. Field and petrographic photographs of the studied Neoproterozoic granites in the southern Yili Block. (a) Neoproterozoic mylonitized granite; (b) Augen and mylonitized granites; (c) Augen granite; (d) Mylonitized granite; (e) Porphyritic gneissic granite; (f) Augen granite (sample WG-5); (g) Mylonitized granite (sample WG-7); (h) Porphyritic gneissic granite (sample KB10). (Per = Perthite; Mi = Microcline; Pl = Plagioclase; Bi = Biotite; Qz = Quartz; Mus = Muscovite).

of the Neoproterozoic meta-sedimentary rocks and metamorphic complexes of the Yili Block have yielded contrasting tectonic models, including interpretations that this block has a similar Precambrian history to that of the Central Tianshan Block (Huang et al., 2016; Huang, 2017; He et al., 2018b), that it originated from the Tarim Craton (Qian et al., 2009; Liu et al., 2014), or that it was an independent microcontinent without tectonic affinity to neighbouring blocks (Hu et al., 2000; Liu et al., 2004).

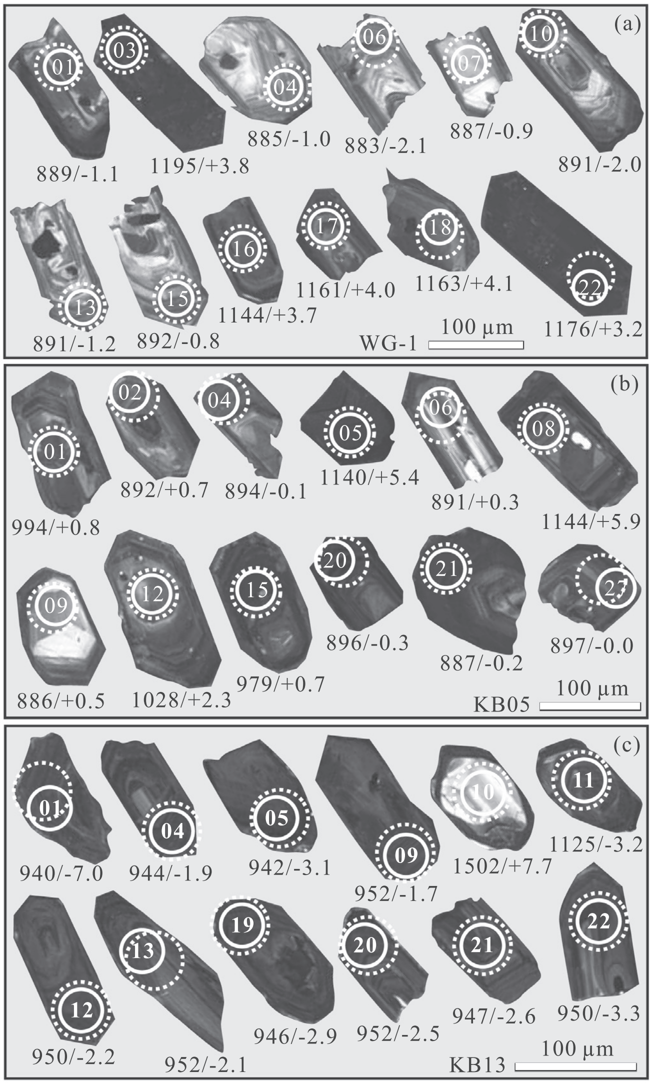

Fig. 4. Representative CL images of zircons from the studied granites in the southern Yili Block. (a) Sample WG-1 from augen granite; (b) KB05 from mylonitized granite; (c) KB13 from gneissic granite. (Solid and dashed circles represent points analysed for U–Pb and Lu–Hf isotopes, respectively).

Here, we document the petrogenesis of Neoproterozoic granitic plutons in the southern Yili Block (Fig. 1) through their petrography, whole-rock geochemistry, Sr–Nd–Hf isotopic compositions, and zircon U–Pb geochronology. Results are integrated with data on Neoproterozoic rocks of the region to outline the tectonic and crustal evolution of the Yili Block and the implications for the evolution of the Rodinia supercontinent.

2. Geological background

The CAOB is bounded by the Baltic Craton to the west, the Siberian Craton to the north, and the combined Tarim–North China cratons to the south (Fig. 1a). The region underwent a complex history spanning the late Mesoproterozoic through late Paleozoic. There are several microcontinents within the southwestern CAOB, including the Central Tianshan Block, the Yili Block, and other Precambrian terranes in Kazakhstan and Kyrgyzstan.

The Yili Block is the easternmost of these Precambrian microcontinents and adjoins the Chu–Yili Block and several other Precambrian blocks in Kazakhstan (Degtyarev et al., 2008; Tretyakov et al., 2015). This block is bordered by the Nalati fault to the south and the North Tianshan fault to the north (Fig. 1b). The Precambrian crystalline and metamorphic basement of the Yili Block crops out along its northern and southern margins (Fig. 1b) and comprises mainly latest Mesoproterozoic to Neoproterozoic amphibolite, gneiss, migmatite, mica schist, marble, and quartzite. The most typical (and studied) basement rocks are those of the Wenquan complex in the northern Yili Block, which includes gneissic granite and migmatite with ages of 987–845 Ma (Hu et al., 2010; Wang et al., 2014a; Huang, 2017) intruded by *ca* 778–776 Ma mafic dykes and associated granite veins (Wang et al., 2014b). The oldest basement rocks exposed in the southern Yili Block are the Meso–Neoproterozoic Tekesi, Kekesu, and Kusitai groups. The Tekesi Group is composed of limestones and dolomites interbedded with quartzites, phyllites, and quartz schists. The Kekesu Group is characterized by thick-bedded grey limestones and dolomites, whereas the Kusitai Group consists mainly of a basal conglomerate grading upward into thin-bedded mudstones and quartz sandstones (XBGMR, 1993; Zhang et al., 2006). These basement units are overlain by late Neoproterozoic to Quaternary sedimentary sequences (Liu et al., 2014) and are intruded by Phanerozoic intrusive rocks with episodes of reworking during Paleozoic orogenesis (Alexeiev et al., 2011; Cao et al., 2017; Huang et al., 2018).

3. Field geology and petrography

Neoproterozoic granites in the southern Yili Block crop out along the Nalati fault near Tekesi City (Fig. 2). These granites intrude the Mesoproterozoic Tekesi Group, which comprises mainly quartz-mica schist, phyllite, quartzite, meta-sandstone, and marble. A series of NNE-trending faults in the southern Yili Block are the major contact boundaries between the Neoproterozoic granites and meta-sedimentary rocks (Fig. 2).

Neoproterozoic augen and mylonitized granites crop out in the western part of the study area (Fig. 2) and have sharp contact relationships without any visible baking or quenching at their margins (Fig. 3a–d). The augen granites are characterized by numerous microcline phenocrysts with a matrix mineral assemblage of microcline (30–35 vol%), perthite (20–25 vol%), oligoclase (5–10 vol%), quartz (25–30 vol%), and biotite (~5 vol%) (Fig. 3f). The mylonitized granites have a fine-grained texture, consisting of microcline (30–35 vol%), perthite (15–20 vol%), oligoclase (5–10 vol%), quartz (20–25 vol%), muscovite (~5 vol%), and biotite (~5 vol%) (Fig. 3g). Some of the augen and mylonitized granites have undergone later sericite alteration. Porphyritic gneissic granites that crop out in the east of the study area are medium to fine grained with phenocrysts of perthite and quartz (Fig. 3e) and are moderately deformed and fractured. The porphyritic gneissic granites comprise perthite (40–45 vol%), oligoclase (10–15 vol%), quartz (25–30 vol%), and biotite (5–10 vol%) with accessory minerals of apatite, zircon, epidote, and opaque mineral oxides (Fig. 3h).

Representative samples were collected for elemental analyses (Fig. 2), including three samples of augen granite (WG-1), mylonitized granite (KB05), and porphyritic gneissic granite (KB13) for zircon dating.

4. Analytical methods

4.1. LA–ICP–MS U–Pb dating of zircons

Zircons were separated using heavy-liquid and magnetic methods. The separated crystals were photographed using an optical microscope, and their internal structures were checked by cathodoluminescence (CL) using an analytical scanning electron microscope (JSM–IT100) connected to a GATAN MINICL system at the State Key Laboratory of Geological Processes and Mineral Resource, China University of Geosciences, Wuhan (GPMR-Wuhan). Imaging conditions included a 10.0–13.0 kV voltage for the electric field and 80–85 μA current for the tungsten filament. The U–Pb isotopic analyses involved laser-

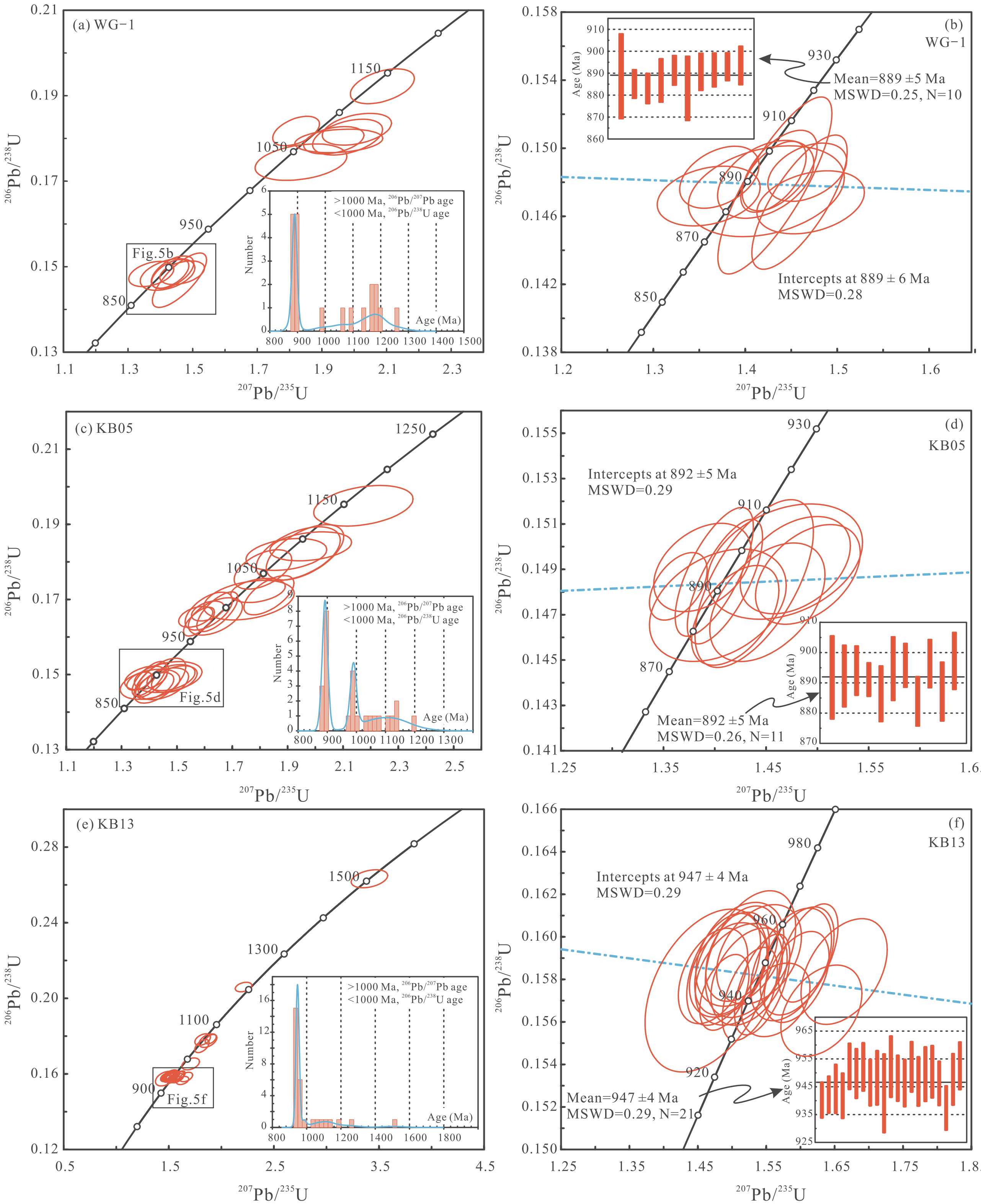

Fig. 5. Zircon U–Pb concordia diagrams for (a) augen granite (WG-1); (b) mylonitized granite (KB05); and (c) gneissic granite (KB13). Inserts are the histograms of zircon age distributions.

ablation–inductively coupled plasma–mass spectrometry (LA–ICP–MS) at the GPMR-Wuhan. A GeolasPro laser-ablation system with a COMPexPro 102 ArF excimer 193 nm laser and a MicroLas optical system were employed with an Agilent 7500a ICP–MS instrument. Laser-ablation spot size, frequency, and energy were set to 32 µm, 6 Hz, and ~60 mJ, respectively. Each analysis incorporated a background acquisition of 20–30 s followed by 50 s of sample data acquisition. Zircon 91,500 was used as the external standard for U–Pb dating and was analysed twice for every six sample analyses, yielding a $^{206}Pb/^{238}U$ age of 1062.9 ± 3.2 Ma (2σ; N = 44; MSWD = 0.04), identical to the age of 1062.4 ± 0.4 Ma recommended by Wiedenbeck et al. (1995). Common Pb correction was not performed because of the low ^{204}Pb

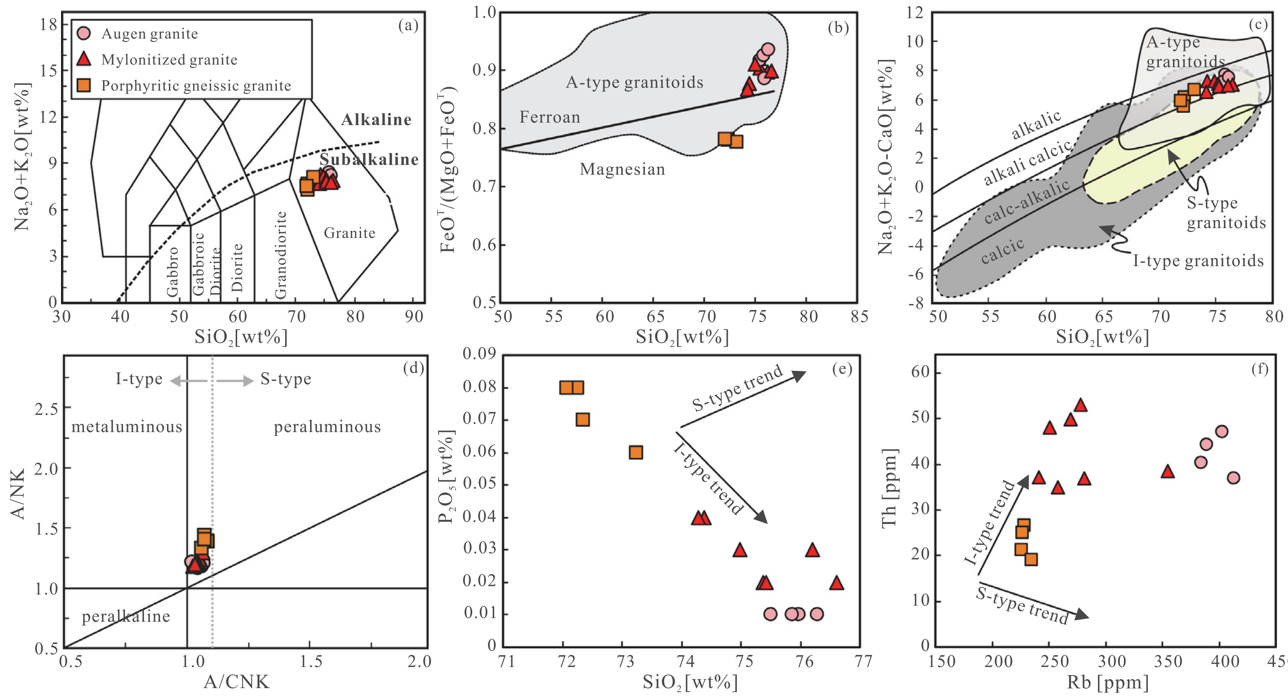

Fig. 6. Variation diagrams for the studied granites of the southern Yili Block. (a) Total-alkali–silica (TAS) classification (Middlemost, 1994); (b) FeO^T/(FeO^T + MgO)– SiO_2 (Frost et al., 2001); (c) (Na_2O + K_2O − CaO)–SiO_2 (Frost et al., 2001); (d) A/NK–A/CNK (Maniar and Piccoli, 1989); (e) P_2O_5–SiO_2; and (f) Th–Rb (Chappell and White, 1992).

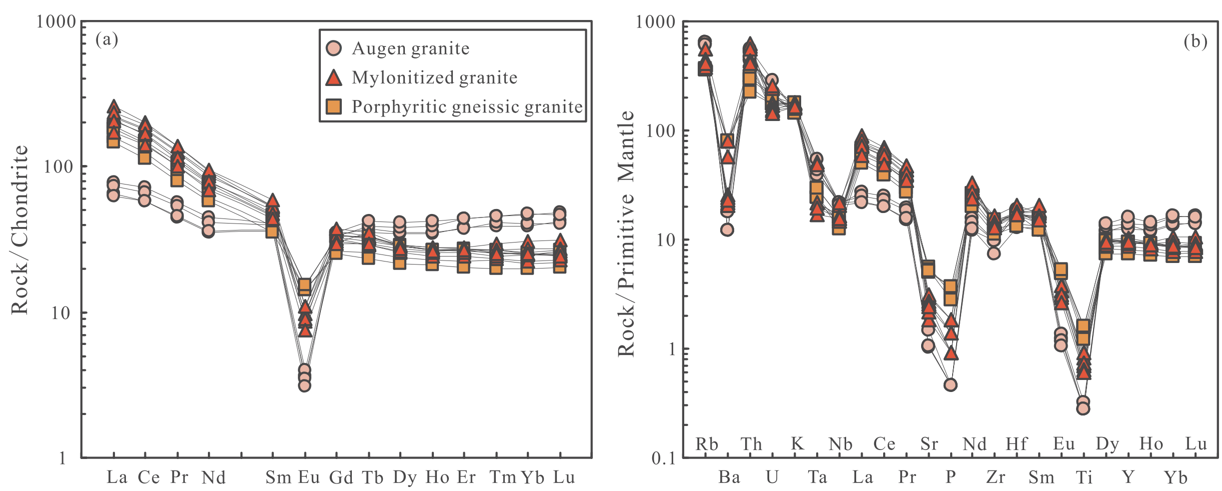

Fig. 7. Chondrite-normalized REE patterns and primitive mantle-normalized trace-element spider diagrams for the studied granites of the southern Yili Block. Normalizing values of chondrite and of primitive mantle are from Taylor and McLennan (1985) and Sun and McDonough (1989), respectively.

signal. Zircon standard GJ-1 was analysed as an unknown, yielding a weighted mean $^{206}Pb/^{238}U$ age of 606.5 ± 5.9 Ma (2σ, N = 8, MSWD = 2.2), which is in good agreement with its recommended age of 608.5 ± 0.4 Ma (Jackson et al., 2004). Concordia diagrams were prepared and weighted mean calculations performed using *Isoplot/Ex_ver3* (Ludwig, 2003). Instrument operating conditions were as described by Liu et al. (2010).

4.2. Zircon Lu–Hf isotopic analyses

In situ zircon Lu–Hf isotopic analyses were performed on dated grains using a Neptune Plus multicollector (MC)–ICP–MS (Thermo Fisher Scientific, Germany) in combination with a Geolas 2005 excimer ArF laser-ablation system (Lambda Physik, Göttingen, Germany) at the GPMR-Wuhan. Analytical spots were close to, or on the top of, spots used for U–Pb analysis, or at least in the same growth domain as inferred from CL images. The laser beam diameter was 44 μm. Each measurement included 20 s background acquisition followed by 50 s of ablation-signal acquisition. Instrument operating conditions were as described by Hu et al. (2012). Off-line selection and integration of analytical signals were performed using *ICPMSDataCal* (Liu et al., 2010). Zircon standards 91,500 and GJ-1 were used to check instrument reliability and stability, yielding weighted mean $^{176}Hf/^{177}Hf$ ratios of 0.282301 ± 0.000010 (2σ, N = 18) and 0.282007 ± 0.000026 (2σ, N = 8), respectively, which are comparable with the recommended values of 0.282308 ± 0.000003 (91500) and 0.282000 ± 0.000005 (GJ-1) (Morel et al., 2008).

4.3. Whole-rock major- and trace-element analyses

Whole-rock samples were crushed in a corundum jaw crusher to 60 mesh. About 60 g was powdered in an agate ring mill to < 200 mesh

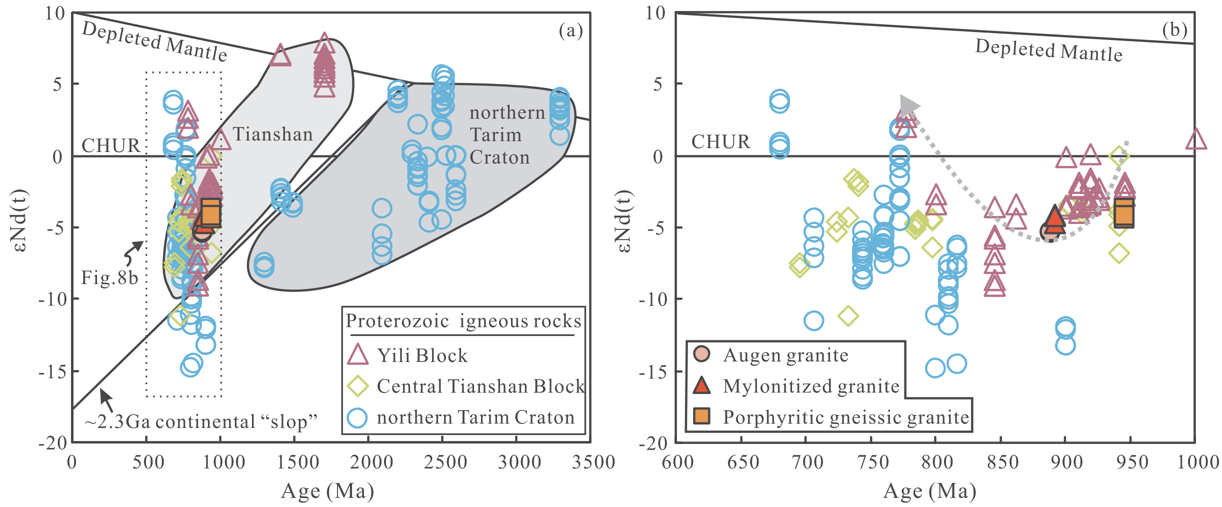

Fig. 8. εNd(t)–Age plots for zircons from Precambrian igneous rocks of this study, from the Yili Block, Central Tianshan Block, and northern Tarim Craton (data from this study; Wang et al. (1991, 2014b,c, 2017); Chen et al. (1999, 2017); Hu et al. (2000, 2010); Zhang et al. (2007b, 2009, 2011, 2012c); Cao et al. (2011); Lei et al. (2013); Ye et al. (2013, 2016); Wu et al. (2014); Cai et al. (2018)).

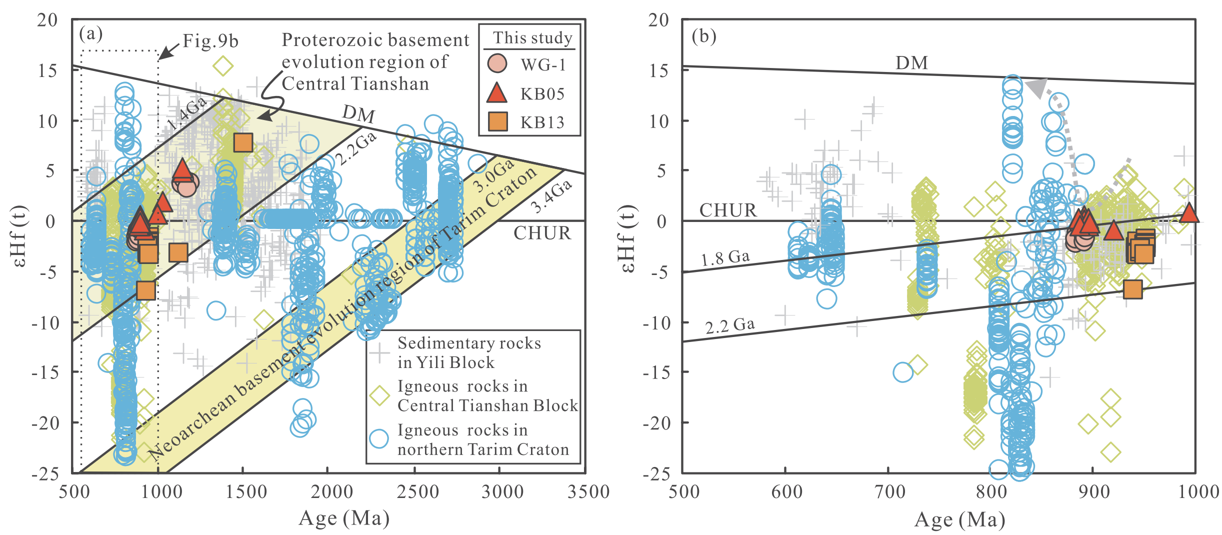

Fig. 9. εHf(t)–Age plots for zircons from Precambrian rocks of the Yili Block, the Central Tianshan Block, and the northern Tarim Craton (data from this study; He et al. (2013, 2015a,b, 2018a); Lei et al. (2013); Ye et al. (2013, 2016); Zong et al. (2013); Ge et al. (2014a, b); Huang et al. (2014, 2015a,b, 2016, 2017); Wang et al. (2014c,d, 2017); Wu et al. (2014, 2018); Gao et al. (2015); Kovach et al. (2016); Chen et al. (2017); Cai et al. (2018)).

for whole-rock geochemical analysis. Major-element analyses involved standard X-ray fluorescence methods using a Shimadzu Sequential 1800 spectrometer at the GPMR-Wuhan. Precision was better than 4% and accuracy better than 3% for major elements. Measurement procedure and data quality were monitored by repeated analyses (one in eight samples) of USGS standard AGV-2 and Chinese National Standards GSR-1 and GRS-7. Analytical techniques were as described by Ma et al. (2012).

Trace-elements were analysed using an Agilent 7500a ICP–MS at the GPMR-Wuhan. Samples were digested in HF + HNO_3 in Teflon bombs. Analyses of USGS standards AGV-2, BHVO-2, BCR-2, and RGM-2 indicate accuracies better than 5%–10% for most trace elements. Sample digestion and ICP–MS instrumental procedures were as described by Liu et al. (2008).

4.4. Whole-rock Sr–Nd isotopic analyses

Sr–Nd isotopic compositions were determined at the GPMR-Wuhan. Sample powders were spiked with mixed isotope tracers, dissolved in HF + HNO_3 in Teflon capsules, and Sr–Nd separated by conventional cation-exchange techniques. Isotopic measurements were performed using a Finnigan MAT-261 thermal-ionization mass spectrometer. Procedural blanks were < 200 pg for Sm and Nd and < 500 pg for Rb and Sr. Mass fractionation corrections for Sr and Nd isotopic ratios were based on $^{86}Sr/^{88}Sr$ = 0.1194 and $^{146}Nd/^{144}Nd$ = 0.7219, respectively. The NBS987 standard measured during the course of the analyses gave a mean $^{87}Sr/^{86}Sr$ ratio of 0.710246 ± 0.000004 (2σ, N = 7), and the Jndi-1 standard gave a mean $^{143}Nd/^{144}Nd$ ratio of 0.512117 ± 0.000003 (2σ, N = 9), which are identical to their recommended values of 0.710241 ± 0.000012 (Thirlwall, 1991) and 0.512115 ± 0.000007 (Tanaka et al., 2000), respectively. Analytical methods, precision, and accuracy are as described by Gao et al. (2004).

5. Results

5.1. Zircon U–Pb geochronology

LA–ICP–MS zircon U–Pb data are given in Supplementary Table S1 and representative zircon CL images with analysis spots are shown in Fig. 4. Although 30 spots were analysed per sample, only those with

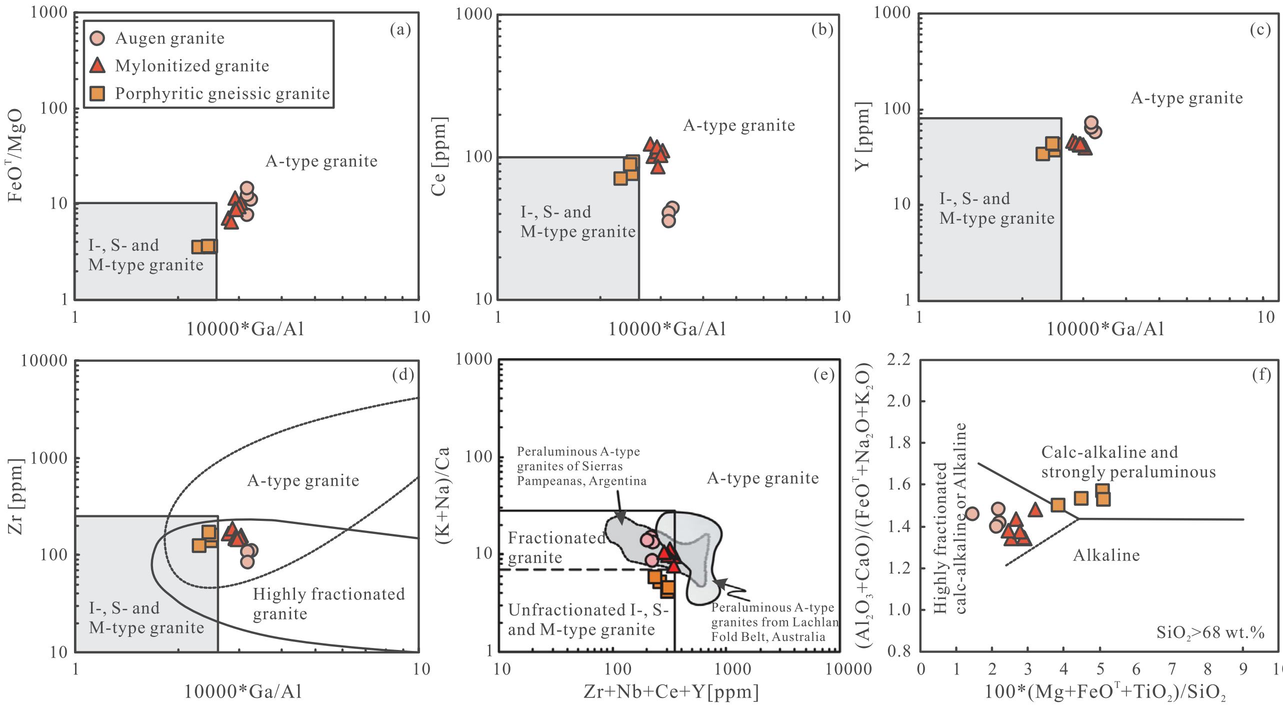

Fig. 10. (a–e) Chemical classification diagrams (after Whalen et al., 1987) in which the augen and mylonitized granites plot in the field of highly fractionated A-type granites; (f) Major-element classification diagram (after Sylvester, 1989) showing the fields of alkaline, calc-alkaline, and highly fractionated calc-alkaline rocks. The fields of A-type and highly fractionated granites in (d) are from Wu et al. (2017); the fields of peraluminous A-type granites are from the following sources: Sierras Pampeanas (Morales Cámera et al., 2017); Lachlan Fold Belt (Whalen et al., 1987).

≥95% concordance were used for interpretation.

Zircons from the augen (sample WG-1) and mylonitized granite (sample KB05) display similar textures and compositions. They are colourless, transparent, or translucent grains. Their lengths are mostly in the range 100–200 μm with aspect ratios of 1:1–3:1. Most grains are euhedral doubly-terminated prismatic crystals with a zoning structure indicative of magmatic origin (Group 1); whereas a few grains are unzoned and dark or exhibit a residual core with corroded margin or zoned rim (Group 2) (Fig. 4a and b). Ten spots in Group 1 of sample WG-1 have concordant $^{206}Pb/^{238}U$ ages of 894–883 Ma (Fig. 5a) with high Th/U ratios (0.21–1.13) and clear oscillatory zoning, confirming their magmatic origin (Hoskin and Schaltegger, 2003). The weighted mean age of 889 ± 2 Ma (MSWD = 0.25, N = 10; Fig. 5b) of these 10 spots is therefore interpreted as the crystallization age of the augen granite. Nine analysed spots from Group 2 (sample WG-1) have concordant $^{206}Pb/^{207}Pb$ ages of 1261–991 Ma (Fig. 5a).

All of the analysed zircons from the mylonitized granite (sample KB05) have high and varied Th (144–982 ppm) and U (277–3352 ppm) contents and high Th/U ratios (0.15–0.89). Group 1 zircons of sample KB05 have concordant $^{206}Pb/^{238}U$ ages of 897–884 Ma with a weighted mean age of 892 ± 5 Ma (MSWD = 0.26, N = 11) (Fig. 5c and d; Supplementary Table S1). Group 2 zircons (KB05) have concordant ages of 1192–979 Ma (Fig. 5c and d).

Zircons from the gneissic granite (sample KB13) are 100–200 μm in length with aspect ratios of 0.25–1.0. Most grains are euhedral crystals with oscillatory or broad zoning, and a few have inherited cores (Fig. 4c). Most analysed spots have concordant $^{206}Pb/^{238}U$ ages of 953–937 Ma (Supplementary Table S1) with a weighted mean age of 947 ± 4 Ma (MSWD = 0.29, N = 21; Fig. 5e and f), interpreted as being the crystallization age of this gneissic granite. Seven analysed spots from the inherited cores have concordant $^{206}Pb/^{207}Pb$ ages of 1502–1039 Ma, implying the occurrence of a previous thermal event.

5.2. Whole-rock geochemistry

Results of bulk-rock major- and trace-element analysis results are given in Supplementary Table S2. All the granites have high SiO_2 (72.1–76.6 wt%) and (K_2O + Na_2O) (7.3–8.4 wt%) contents and high A/CNK ratios (1.03–1.09; modal $Al_2O_3/(CaO + Na_2O + K_2O)$), indicating a calc-alkaline, weakly peraluminous affinity (Fig. 6a–d). The gneissic granites have low FeO^T/MgO ratios (3.49–3.59) and high $Mg^\#$ values (33–34; modal 100*Mg/(Mg + Fe)), and therefore resemble magnesian granites (Frost and Frost, 2011). The augen- and mylonitized granites have contrasting FeO^T/MgO ratios (6.52–14.58) and $Mg^\#$ values (11–21) to those of the gneissic granites, defining a ferroan granite trend (Fig. 6b).

In chondrite-normalized rare earth elements (REEs) diagrams (Fig. 7a), the gneissic granites exhibit enrichment in light REEs (LREEs) with $(La/Yb)_N$ ratios of 7.21–7.70, strong negative Eu anomalies (δEu = 0.37–0.47), and significant differentiation of LREEs ($(La/Sm)_N$ = 3.96–4.06). The mylonitized granites have REEs patterns similar to those of the gneissic granites with ratios $(La/Yb)_N$ = 6.86–10.01, $(La/Sm)_N$ = 3.84–4.73, and δEu = 0.20–0.25. In contrast, the augen granites display flat REEs patterns with low $(La/Yb)_N$ (1.32–1.92) and $(La/Sm)_N$ (1.66–1.89) ratios (Fig. 7a). All of the granites are characterized by depletion of Nb, Ta, Ba, Sr, P, Eu, and Ti, strong enrichment in large-ion lithophile elements (LILEs), and highly differentiated high field strength elements (HFSEs) in their primitive mantle-normalized trace element patterns (Fig. 7b).

5.3. Sr–Nd–Hf isotopes

Whole-rock Sr and Nd isotopic compositions are presented in Supplementary Table S3. Initial Sr and Nd isotopic ratios and εNd(t) values of these granites were calculated using their crystallization ages. The studied granites all show identical Nd isotopic compositions characterized by relatively low initial $^{143}Nd/^{144}Nd$ ratios of 0.511190–0.511275 and εNd(t) values of −5.44 to −3.75. The augen

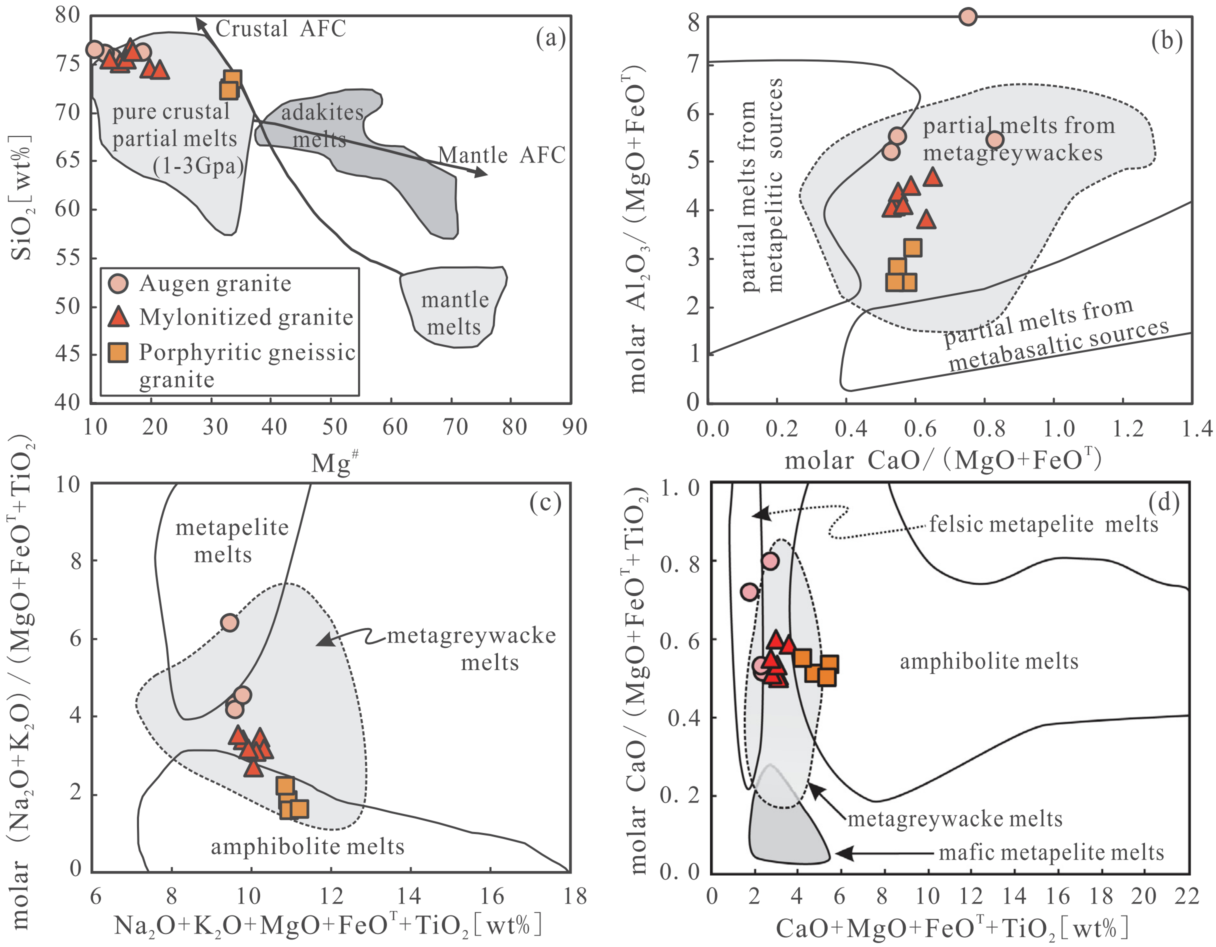

Fig. 11. Chemical compositions of the studied granites of the southern Yili Block. Outlined fields denote compositions of partial melts obtained in experimental studies by dehydration melting of various bulk compositions. The curves of mantle AFC and crustal AFC are after Stern and Kilian (1996). (Data sources: Vielzeuf and Holloway, 1988; Patiño Douce and Johnston, 1991; Rapp and Watson, 1995; Patiño Douce and Beard, 1996).

and mylonitized granites display a wide variation in initial $^{87}Sr/^{86}Sr$ ratios (0.703921–0.745403), whereas the gneissic granites have a relatively narrow range (0.718526–0.723162). As the Nd–Hf isotopic compositions (presented below) are relatively uniform, the abnormally high and low initial $^{87}Sr/^{86}Sr$ ratios of the augen and mylonitized granites (0.743550–0.745403 and 0.703921, respectively) may reflect the influence of low grades of deformation and metamorphism (Barovich and Patchett, 1992; Ma and Liu, 2001). These data were therefore excluded from the discussion of petrogenesis. All of the granites have similar Nd model ages (T_{2DM}) of 1.96–1.88 Ga, similar to the age of basement rocks in the Tianshan Block (Fig. 8; Hu et al., 2000; Kröner et al., 2017; Wang et al., 2017).

In situ zircon Lu–Hf isotopic data are given in Supplementary Table S4. Zircons from the augen granites (sample WG-1), with a $^{206}Pb/^{238}U$ age of 889 Ma, display a uniform isotopic composition with εHf(t) values of − 2.11 to − 0.76. The ca. 892 Ma zircons from the mylonitized granites (sample KB05) have slightly higher εHf(t) values of −0.26 to 0.72. Old inherited zircons from the augen and mylonitized granites have positive εHf(t) values of 3.16–4.09 and 0.70–5.90, respectively (Fig. 9a). Nonetheless, the magmatic and inherited zircons from the two granites have similar two-stage Hf model ages of 1.91–1.60 Ga. In contrast, the gneissic granites (sample KB13) have much lower initial $^{176}Hf/^{177}Hf$ ratios (0.282005–0.282158) and εHf(t) values (−6.95 to − 1.67) as well as older Hf model ages (2.26–1.93 Ga) (Fig. 9b). However, two analyses of inherited zircon cores (ca. 1502 Ma and 1125 Ma) from sample KB13 yielded varied Hf isotopic compositions with εHf(t) values of +7.74 and −3.19 and two-stage Hf model ages of 1.76 and 2.17 Ga.

6. Discussion

6.1. Petrogenesis of the two granite groups of the Yili Block

Zircon U–Pb dating reveals two periods of Neoproterozoic granitic magmatism in the southern Yili Block, represented by the ca. 947 Ma gneissic granite in the eastern part of the study area and the ca. 890 Ma augen and mylonitized granites in the western part. The gneissic granites are magnesian with higher $Mg^{\#}$ values (33–34) than those of the augen and mylonitized granites ($Mg^{\#}$ = 11–21) and belong to the ferroan granite series (Fig. 6b). This contrast indicates different potential source regions and/or petrogenetic processes. The absence of Al-rich minerals, low A/CNK ratios (< 1.1), negative correlation between P_2O_5 and SiO_2, and positive correlation between Th and Rb preclude the gneissic granites from being S-type granites (Figs. 3 and 6; Chappell and White, 1992; Chappell, 1999). Furthermore, the gneissic granites have low Ga/Al and FeO^T/MgO ratios and high MgO, FeO^T, and TiO_2 contents, and therefore resemble calc-alkaline, weakly peraluminous I-type granites (Whalen et al., 1987; Fig. 10). In contrast, the augen and mylonitized granites have high SiO_2 (> 74 wt%) and alkali ($Na_2O + K_2O$ = 7.70–8.39 wt%) contents, high FeO^T/MgO and 10000*Ga/Al (> 2.8) ratios, and low CaO, Al_2O_3, Ba, and Sr contents, indicating a similarity to highly fractionated calc-alkaline A-type granites (Whalen et al., 1987; Frost and Frost, 2011; Wu et al., 2017; Fig. 10).

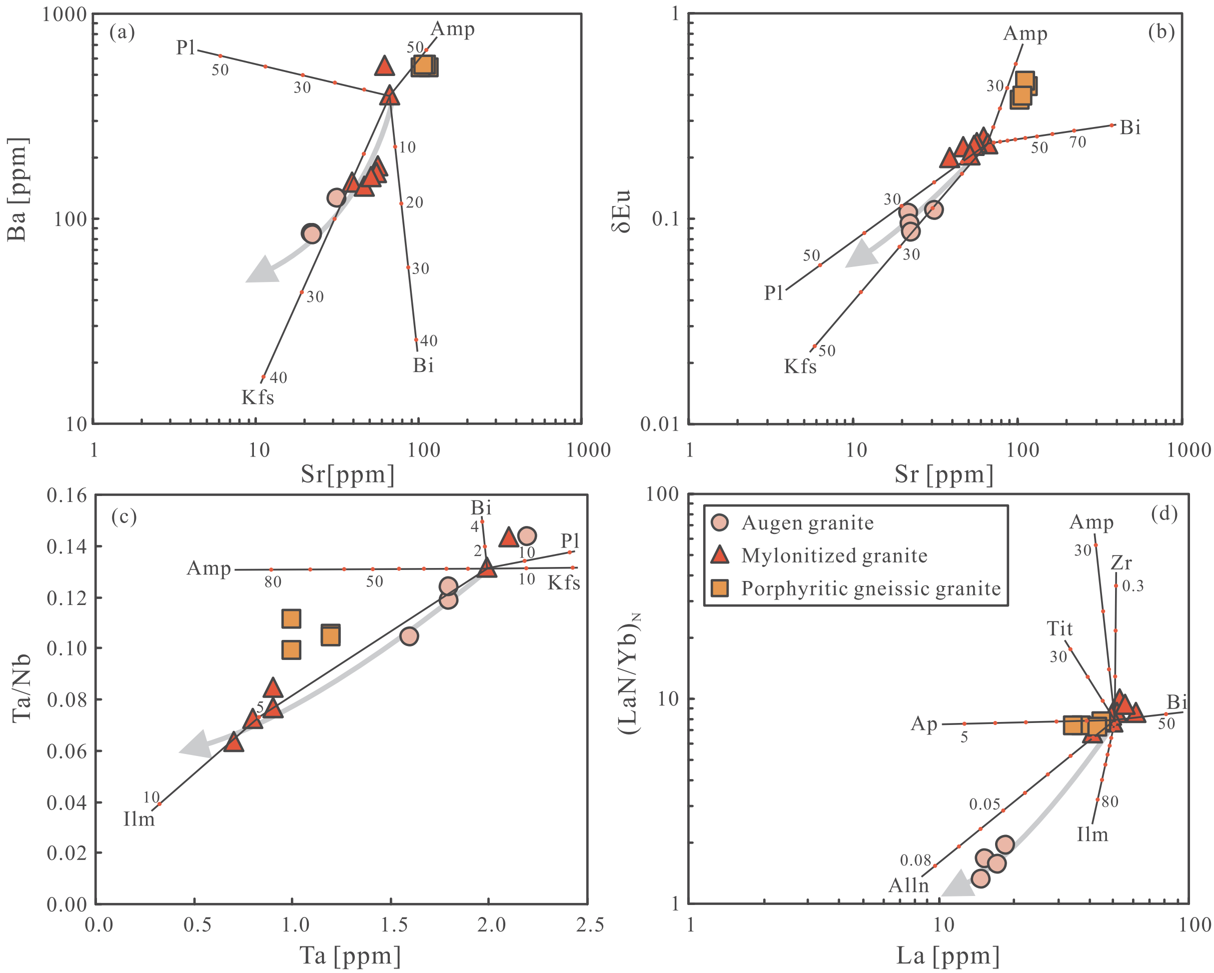

Fig. 12. Diagrams of fractional crystallization simulation (Ersoy and HelvacI, 2010). (a) Ba–Sr; (b) δEu–Sr; (c) Ta/Nb–Ta; (d) $(La/Yb)_N$–La. Pl = plagioclase; Kfs = K-feldspar; B = biotite; Amp = amphibole; Ap = apatite; Alln = allanite; Ilm = ilmenite; Tit = titanite; Zr = zircon.

Compared with results of experimental petrological studies (Fig. 11), all the samples have high SiO_2 contents, high K_2O/Na_2O and $Al_2O_3/(MgO + FeO^T)$ ratios, moderate $CaO/(MgO + FeO^T)$ and $(Na_2O + K_2O)/(MgO + FeO^T + TiO_2)$ ratios, relatively low $Mg^{\#}$ and $(MgO + FeO^T + TiO_2)$ values, low εNd(t) values (−5.44 to −3.75), and high initial $^{87}Sr/^{86}Sr$ ratios (0.716530–0.720543 and 0.718526–0.723162 for ca. 890 Ma and ca. 947 Ma granites, respectively). These geochemical characteristics suggest a derivation from the partial melting of crustal metagreywackes (Patiño Douce and Johnston, 1991; Patiño Douce and Beard, 1996). The following observations indicate that there is no unequivocal evidence for a contribution of mantle materials: (1) an addition of mafic components would produce rocks with moderate SiO_2 contents (Stern and Kilian, 1996); (2) the mantle has high Zr/Hf (34–42) and Nb/Ta (14.2–15.9) ratios (Sun and McDonough, 1989; Green, 1995), and an addition of mantle materials would enhance those ratios, which is not the case for the studied granites; and (3) there is no diorite–granodiorite–granite association in the studied area, which is inconsistent with a magma mixing and/or fractional crystallization model.

Notably, the gneissic granites have older model ages (ca. 2.0 Ga) and much higher $Mg^{\#}$ values than those of the augen and mylonitized granites at the same SiO_2 contents, which indicates that the source of the gneissic granites was relatively enriched in MgO. In contrast, the chondrite-like εHf(t) values (−2.11 to 0.72) and relatively young Hf model ages of the ca. 890 Ma augen and mylonitized granites suggest their derivation from ca. 1.8 Ga metagreywackes with a weak juvenile crust signature. This conclusion is consistent with results of studies of Precambrian basement rocks of the Yili Block (e.g., Wenquan complex and Kailaketi Group), in which the amphibolites and meta-sedimentary rocks display an obvious age peak at ca. 1.8–1.7 Ga with high positive εNd(t) and εHf(t) values (Figs. 8a and 9a), thereby indicating the presence of late Paleoproterozoic juvenile crustal materials (Hu et al., 2000; He et al., 2015a; Huang et al., 2016). In addition, the occurrence of small amounts of inherited zircons (1502–979 Ma; Fig. 5; Supplementary Table S1) indicates a minor contribution of Mesoproterozoic rocks to the petrogenesis of the studied granites.

Furthermore, the contrast in REE distribution patterns between the augen ($(La/Yb)_N$ = 1.24–1.81) and mylonitized granites ($(La/Yb)_N$ = 6.46–9.43) indicates that fractionation also played an important role in producing their chemical variations. This is further confirmed by their marked negative Eu, Ba, Sr, Na, Ta, P, and Ti anomalies (Fig. 7). Through geochemical modelling (Ersoy and HelvacI, 2010), the main fractionating phases of K-feldspar, plagioclase, and biotite may be included in our samples, as indicated by the positive Ba–Sr and δEu–Sr correlations (Fig. 12a and b). As shown in Fig. 12, the negative Na, Ta, P and Ti, anomalies can be interpreted as reflecting fractionation of ilmenite, allanite, and possibly apatite, with such fractionation also being consistent with their petrographic features (Fig. 3).

6.2. Implications for the early Neoproterozoic tectonic evolution of the Yili Block

The magma sources and processes involved in the generation of

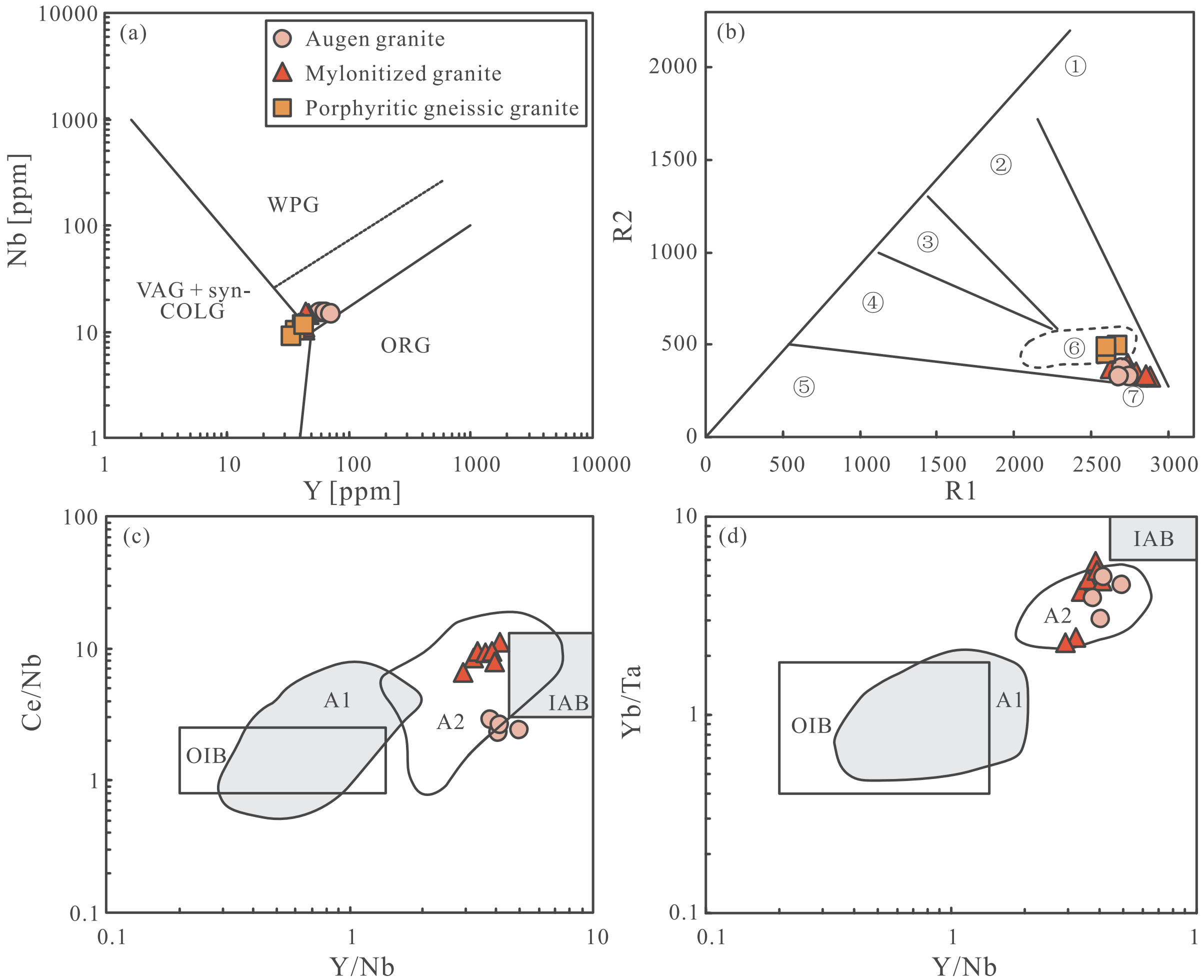

Fig. 13. Trace- and major-element discrimination diagrams for the tectonic setting of the studied granites. (a) Nb–Y (Pearce et al., 1984); (b) R1–R2 diagram of Batchelor and Bowden (1985): (1) mantle fractionates, (2) pre-plate collision, (3) post-collision, (4) late orogenic, (5) anorogenic, (6) syn-collision, and (7) post-orogenic; (c, d) Chemical subdivision of A-type granites (Eby, 1992), (A1) truly anorogenic rifting; (A2) post-collisional.

granites, as reflected by their geochemical signatures, show a significant correlation with tectonic settings (Pearce, 1996). The bulk-rock major- and trace-element compositions of the ca. 947 Ma gneissic granites of the Yili Block resemble those of syn-collisional granites (Fig. 13), whereas the ca. 890 Ma granites display geochemical affinities similar to those of extension-related granites. The ca. 890 Ma granites have high Y/Nb and Yb/Ta ratios (Fig. 13c and d) similar to those of A2-type granites (Eby, 1992), indicating that their petrogenesis is related to post-collisional extension, as for many highly fractionated granitoids.

The ages and tectonic interpretations for the analysed samples are in accordance with data from regional magmatism and metamorphism in the Yili Block and adjacent blocks within the CAOB. These blocks are characterized by large-scale linearly distributed ca. 1000–890 Ma I- and S-type granitoids (Figs. 1b, 14, and 15). Such trends resemble those convergent, continental margin accretionary orogens and may therefore have been related to the assembly of Rodinia. Some I-type granitoids within these CAOB blocks display high-K calc-alkaline and arc-related geochemical characteristics with enrichment in LREEs and LILEs and depletion of HREEs and HFSEs as observed, for example, in 945 ± 22 Ma biotite granites in Aktau–Yili (Tretyakov et al., 2015), 969 ± 11 Ma granitic gneisses in Chinese Central Tianshan (Yang et al., 2008), and 1045 ± 7 Ma granites in the southern part of Kazakhstan North Tianshan (Kröner et al., 2013). This further confirms the presence of latest Mesoproterozoic to earliest Neoproterozoic subduction-related magmatism in these blocks, which were assembled within the current southwestern CAOB. Furthermore, as shown in Fig. 5, inherited zircons from the studied granites also record a latest Mesoproterozoic to earliest Neoproterozoic tectono-magmatic event, with an age peak of ca. 985 Ma recorded in sample KB05. Subsequent tectono-magmatic activities, including anatexis-related migmatization (926–909 Ma) of basement rocks (i.e., Wenquan Group), S-type granitic magmatism (919–909 Ma), mylonitization (ca. 919 Ma), and greenschist- to amphibolite-facies metamorphism of early Neoproterozoic gneisses, are recognized in the northern Yili Block (Hu et al., 2010; Wang et al., 2014a; Huang, 2017). Such tectonic features are commonly linked to collisional orogenesis (e.g., Brown, 2007; Liou et al., 2009), thus indicating that the Yili Block occupied a syn-collisional setting during ca. 950–900 Ma. The 947–890 Ma granitoids of the Yili Block are mainly I- and S-type, whereas the 890–800 Ma granitoids are mainly A-type (Fig. 15). This shift in characteristics (Supplementary Table S5) likely reflects a tectonic transition from syn-collisional to post-collisional extension associated with Neoproterozoic orogenesis in this region of the CAOB.

Large-scale I- and S-type granitic magmatism in the Yili and adjacent Central Tianshan blocks were synchronous at 960–900 Ma (Fig. 14), indicating a similar history during the early Neoproterozoic. The termination of these igneous activities corresponds to ca. 900 Ma peak high-grade metamorphism in the southwestern CAOB (Wang et al., 2014a; Huang, 2017; Zong et al., 2017). This tectonic transition has also been recorded in Meso–Neoproterozoic strata (i.e., the Tekesi and Kusitai groups) in the southern Yili Block. The Tekesi Group marine

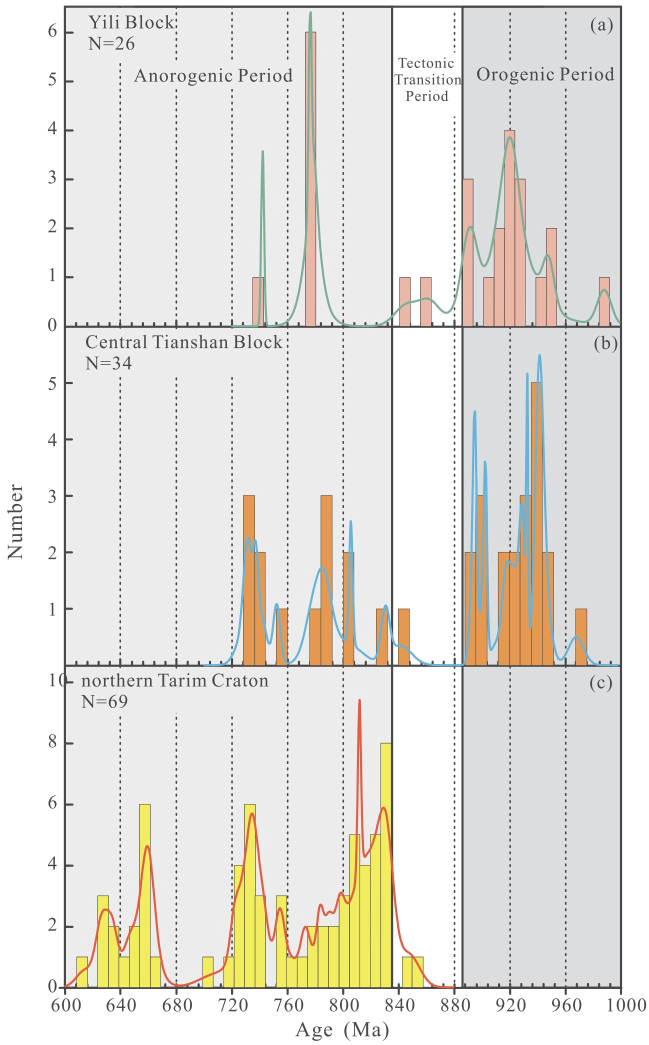

Fig. 14. Zircon U–Pb age frequency distributions for Neoproterozoic igneous rocks of the Yili Block, Central Tianshan Block, and Tarim Craton (data sources: Supplementary Table S5).

sedimentary sequence is unconformably covered by the Kusitai Group and later Neoproterozoic sedimentary cover comprising mainly terrestrial clastic rocks and interlayered glacial deposits (XBGMR, 1993; Zhang et al., 2006; Ding et al., 2009). Our recent research revealed that the Tekesi Group was deposited during the latest Mesoproterozoic to earliest Neoproterozoic (1040–960 Ma) and that the Kusitai Group accumulated during the early Neoproterozoic (< 926 Ma) (Huang et al., 2019). The regional stratigraphic unconformity and contrasting rock assemblages between these units may reflect the suggested tectonic transition.

After the transition from a syn-collisional to a post-collisional setting, the Yili Block and nearby blocks within the CAOB evolved to a post-orogenic extension regime. A later stage of continental rifting in the southwestern CAOB may have occurred as early as ca. 830 Ma, as documented by mafic dyke swarms, composite volcanic flows, and bimodal intrusions (Zhang et al., 2007a, 2012b; Lu et al., 2008; Chen et al., 2017). These indications of rifting may mark the onset of the separation of the southwestern CAOB during the break-up of the Rodinia supercontinent (Li et al., 2008; Cawood et al., 2018).

6.3. *Crustal reworking and tectonic affinity of the Yili Block during the Neoproterozoic*

The studied Neoproterozoic granites have enriched Nd–Hf isotopic compositions, characterized by negative εNd(t) values (−3.75 to −4.45 for the ca. 947 Ma gneissic granites; −4.14 to −5.44 for the ca. 890 Ma augen and mylonitized granites) and negative or chondrite-like εHf(t) values (−6.95 to −1.67 for ca. 947 Ma gneissic granites; −2.11 to 0.72 for ca. 890 Ma granites). Nd–Hf crustal model ages vary within a narrow range with peaks at 2.0 Ga for the ca. 947 Ma gneissic granites, and 1.8 Ga for the ca. 890 Ma granites. The Nd–Hf model ages (Figs. 8a and 9a) recorded here and in other studies of the sedimentary provenance of Paleoproterozoic detrital zircons (e.g., Liu et al., 2014; Huang et al., 2016; Huang, 2017) reveal that the Yili Block may have a Paleoproterozoic basement. The studied granites have marked negative whole-rock εNd(t) and zircon εHf(t) values (Figs. 8 and 9), indicating that reworking of old continental crust was the major mechanism for the Neoproterozoic crustal evolution of the Yili Block.

Inherited zircons (1502–979 Ma) in the studied granites have high positive εHf(t) values (0.70–7.74; Fig. 9a; Supplementary Table S4), barring spot KB13-11 with an age of 1125 Ma and εHf(t) value of −3.19. Most inherited zircons are euhedral with high Th/U ratios of 0.14–1.16, with some grains displaying bright cores with oscillatory zoning surrounded by dark overgrown rims (Fig. 4), indicating magmatic origins. These features, together with results of studies of Mesoproterozoic detrital zircons in the Yili Block (Fig. 9a), suggest that Mesoproterozoic crustal growth events in the Yili Block correspond to 1450–1400 Ma and 1150–1050 Ma magmatic events that occurred in the southern CAOB (e.g., Kröner et al., 2013; He et al., 2018a).

Nd–Hf isotopic compositions of the igneous rocks follow an enriched trend during the period 1000–890 Ma (Figs. 8 and 9), suggesting that crustal reworking played a major role in the evolution of the Yili Block. However, there were multiple crustal growth events after ca. 890 Ma, with the earliest pulse from ca. 830 to 800 Ma being followed by those at ca. 780–720 Ma and 650–630 Ma. These events echo the episodic rifting activity related to the break-up of the Rodinia supercontinent (Zhang et al., 2012b; Han et al., 2018). The evolution from crustal reworking to multiple pulses of juvenile crustal growth is also recorded in Neoproterozoic meta-sedimentary rocks from the Yili Block, in which detrital zircons with ages of 1000–890 Ma display enriched Lu–Hf isotopic compositions, but those with ages < 800 Ma are mostly isotopically depleted. This Lu–Hf isotopic feature is consistent with the Nd isotopic trend of Neoproterozoic igneous rocks in the Yili Block (Fig. 8) and likely reflects a change in the process of crustal evolution.

The Nd–Hf isotopic compositions of the studied granites as well as their inherited zircons indicate that the Yili Block has a basement history and tectonic evolution similar to that of the Central Tianshan Block, in which the 2.2–1.8 Ga Paleoproterozoic basement also underwent juvenile crustal growth during the Mesoproterozoic (Figs. 8 and 9). The tectonic affinities of early Neoproterozoic magmatism in the Yili and adjacent blocks in the southwestern CAOB suggest that they were at or near an active continental margin during the assembly of Rodinia. The situation may have been similar to the Cenozoic orogens of the Tethyan margin of Tibet and to the Andes margin of South America.

In contrast, the Tarim Craton has an Archean basement and lacks evidence for orogeny-related magmatism during 1.0–0.9 Ga and subsequent high-grade metamorphism (ca. 900 Ma) (e.g., Cai et al., 2018; Yang et al., 2018). These differences in basement age and latest Mesoproterozoic–early Neoproterozoic magmatism preclude the possibility that the Yili Block was part of the Tarim Craton during much of the Proterozoic. Furthermore, the absence of Neoarchean to early Paleoproterozoic magmatism in the Yili Block, in contrast to their occurrence in the Tarim Craton (Figs. 8 and 9), suggests that these two blocks, which are now adjacent, had independent and spatially unrelated histories from the Archean through to the early Neoproterozoic. After ca. 890 Ma, the Tarim Craton had a similar magmatic record to that of the Yili and Precambrian blocks in the southwestern CAOB, characterized by I- and A-type but no S-type granitoids, as well as coeval < 830 Ma rifting-related magmatic rocks (such as mafic dyke swarms, mafic and alkaline complexes, and bimodal igneous rocks) (Zhang et al., 2007a,

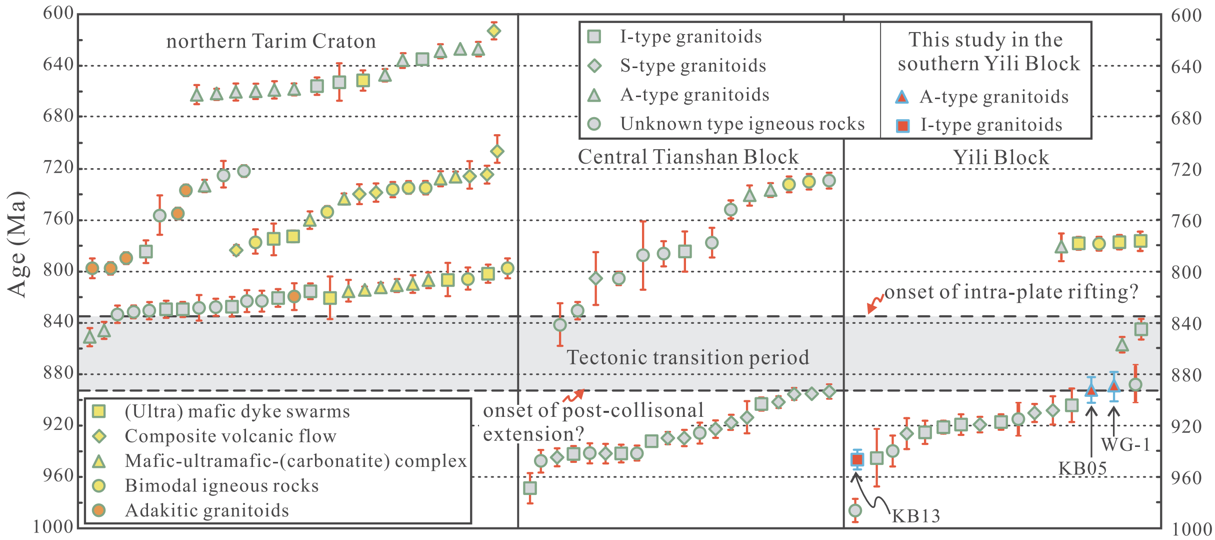

Fig. 15. Diagram illustrating the distribution of the Neoproterozoic magmatism in different genetic types from the Yili Block, Central Tianshan Block, and northern Tarim Craton (Data sources: Supplementary Table S5).

2012b, 2013; Lu et al., 2008; Ye et al., 2013; Wang et al., 2014b; Chen et al., 2017). These features indicate that all of these Precambrian blocks were likely spatially associated by ca. 830 Ma during the break-up of the margin of the Rodinia supercontinent.

In summary, the Yili Block has a geological history similar to that of the Central Tianshan Block but differed from that of the Tarim Craton until the final assembly of the Rodinia supercontinent. During the early Neoproterozoic (1000–890 Ma), the Yili Block and Central Tianshan Block represented an Andean-type orogen with the generation of numerous I- and S-type granitoids, in which the reworking of ancient continental crust played a major role in their crustal evolution. In contrast, coeval magmatic records are rare in the Tarim Craton. By the middle Neoproterozoic (not later than 830 Ma), rifting-related magmatism may have marked the end of the early Neoproterozoic orogeny and the beginning of intra-plate tectonic systems.

7. Conclusions

Several conclusions can be drawn from this study of the petrography, geochemistry, and geochronology of Neoproterozoic granitic plutons in the southern Yili Block and from the synthesis of other studies of Precambrian blocks in the southwestern CAOB, as follows.

(1) I-type granites dated at ca. 947 Ma and highly fractionated A-type granites dated at ca. 892–889 Ma occur in the southern Yili Block and were derived from the partial melting of ca. 2.0 Ga MgO-rich basement rocks and from a ca. 1.8 Ga crustal source, respectively. This suggests that crustal reworking played a major role in the early Neoproterozoic crustal evolution of the Yili Block.
(2) The Yili Block experienced a tectonic transition from *syn*-collisional to post-collisional extension at ca. 890 Ma, after which the tectonic setting evolved gradually to orogenic intra-plate rifting during the late Tonian.
(3) The Yili Block shares a similar tectonic affinity and evolutionary history to that of the Central Tianshan Block but different from that of the Tarim Craton. The Yili and Central Tianshan blocks were probably part of an early Neoproterozoic orogenic system that developed along the exterior margin of the Rodinia supercontinent.

Acknowledgements

We sincerely thank editor G.C. Zhao, reviewer Kirill E. Degtyarev, and two anonymous reviewers for their constructive comments and suggestions, which substantially improved our manuscript. This study was financially supported by the 973 Program (2015CB453000), the National Natural Science Foundation of China (41602049), and the China Postdoctoral Science Foundation (2015M582529). Cawood acknowledges support from the Australian Research Council Grant FL160100168. Ducea acknowledges support from US National Science Foundation Grant EAR 1725002 and the Romanian Executive Agency for Higher Education, Research, Development and Innovation Funding (PN-III-P4-ID-PCE-2016-0127 and PN-III-P4-ID-PCCF-2016-0014).

Appendix A. Supplementary data

Supplementary data to this article can be found online at https://doi.org/10.1016/j.precamres.2019.04.017.

References

Alexeiev, D.V., Ryazantsev, A.V., Kröner, A., Tretyakov, A.A., Xia, X., Liu, D.Y., 2011. Geochemical data and zircon ages for rocks in a high-pressure belt of Chu-Yili Mountains, southern Kazakhstan: implications for the earliest stages of accretion in Kazakhstan and the Tianshan. J. Asian Earth Sci. 42 (5), 805–820.

Barovich, K.M., Patchett, P.J., 1992. Behavior of isotopic systematics during deformation and metamorphism: a Hf, Nd and Sr isotopic study of mylonitized granite. Contrib. Miner. Petrol. 109 (3), 386–393.

Batchelor, R.A., Bowden, P., 1985. Petrogenetic interpretation of granitoid rock series using multicationic parameters. Chem. Geol. 48 (1–4), 43–55.

Brown, M., 2007. Crustal melting and melt extraction, ascent and emplacement in orogens: mechanisms and consequences. J. Geol. Soc. 164 (4), 709–730.

Cai, Z., Xu, Z., Yu, S., Li, S., He, B., Ma, X., Chen, X., Xu, X., 2018. Neoarchean magmatism and implications for crustal growth and evolution of the Kuluketage region, northeastern Tarim Craton. Precambr. Res. 304, 156–170.

Cao, X., Lü, X., Liu, S., Zhang, P., Gao, X., Chen, C., Mo, Y., 2011. LA-ICP-MS zircon dating, geochemistry, petrogenesis and tectonic implications of the Dapingliang Neoproterozoic granites at Kuluketage block, NW China. Precambr. Res. 186, 205–219.

Cao, Y., Wang, B., Jahn, B., Cluzel, D., Shu, L., Zhong, L., 2017. Late Paleozoic arc magmatism in the southern Yili Block (NW China): insights to the geodynamic evolution of the Balkhash-Yili continental margin, Central Asian Orogenic Belt. Lithos 278, 111–125.

Cawood, P.A., Kröner, A., Collins, W.J., Kusky, T.M., Mooney, W.D., Windley, B.F., 2009. Accretionary orogens through Earth history. Geol. Soc., London, Spec. Publ. 318, 1–36.

Cawood, P.A., Zhao, G., Yao, J., Wang, W., Xu, Y., Wang, Y., 2018. Reconstructing South China in Phanerozoic and Precambrian supercontinents. Earth Sci. Rev. 186, 173–194.

Chappell, B.W., 1999. Aluminium saturation in I- and S-type granites and the characterization of fractionated haplogranites. Lithos 46, 535–551.

Chappell, B.W., White, A.J.R., 1992. I-and S-type granites in the Lachlan Fold Belt. Trans. R. Soc. Edinburgh: Earth Sci. 83, 1–26.

Chen, H., Chen, Y., Ripley, E.M., Li, C., Deng, X., Yue, S., Zheng, Z., Fu, B., 2017. Isotope and trace element studies of the Xingdi II mafic–ultramafic complex in the northern rim of the Tarim Craton: evidence for emplacement in a Neoproterozoic subduction zone. Lithos 278, 274–284.

Chen, Y.B., Hu, A.Q., Zhang, G.X., Zhang, Q.F., 1999. Zircon U-Pb age and Nd-Sr isotopic composition of granitic gneiss and its geological implications from Precambrian window of western Tianshan, NW China. Geochimica 28, 515–520.

DeCelles, P.G., Ducea, M.N., Kapp, P., Zandt, G., 2009. Cyclicity in Cordilleran orogenic systems. Nat. Geosci. 2 (4), 251–257.

Degtyarev, K.E., Shatagin, K.N., Kotov, A.B., Sal Nikova, E.B., Luchitskaya, M.V., Tret Yakov, A.A., Yakovleva, S.Z., 2008. Late Precambrian volcanoplutonic association of the Aktau-Dzhungar massif, Central Kazakhstan: Structural position and age. Dokl. Earth Sci. 421 (2), 879–883.

Degtyarev, K., Yakubchuk, A., Tretyakov, A., Kotov, A., Kovach, V., 2017. Precambrian geology of the Kazakh uplands and Tien Shan: an overview. Gondwana Res. 47, 44–75.

Ding, H.F., Ma, D.S., Yao, C.Y., Shu, L.S., 2009. Sedimentary environment of Ediacaran glaciogenic diamictite in Guozigou of Xinjiang, China. Chin. Sci. Bull. 54 (18), 3283–3294.

Eby, G.N., 1992. Chemical subdivision of the A-type granitoids: petrogenetic and tectonic implications. Geology 20, 641–644.

Ersoy, Y., HelvacI, C., 2010. FC-AFC-FCA and mixing modeler: a Microsoft Excel(c) spreadsheet program for modeling geochemical differentiation of magma by crystal fractionation, crustal assimilation and mixing. Comput. Geosci. 36 (3), 383–390.

Frost, B.R., Barnes, C.G., Collins, W.J., Arculus, R.J., Ellis, D.J., Frost, C.D., 2001. A geochemical classification for granitic rocks. J. Petrol. 42 (11), 2033–2043.

Frost, C.D., Frost, B.R., 2011. On ferroan (A-type) granitoids: their compositional variability and modes of origin. J. Petrol. 52 (1), 39–53.

Gao, S., Rudnick, R.L., Yuan, H.L., Liu, X.M., Liu, Y.S., Xu, W.L., Ling, W.L., Ayers, J., Wang, X.C., Wang, Q.H., 2004. Recycling lower continental crust in the North China craton. Nature 432 (7019), 892–897.

Gao, J., Wang, X.S., Klemd, R., Jiang, T., Qian, Q., Mu, L.X., Ma, Y.Z., 2015. Record of assembly and breakup of Rodinia in the Southwestern Altaids: evidence from Neoproterozoic magmatism in the Chinese Western Tianshan Orogen. J. Asian Earth Sci. 113, 173–193.

Ge, R., Zhu, W., Wilde, S.A., He, J., Cui, X., Wang, X., Bihai, Z., 2014a. Neoproterozoic to Paleozoic long-lived accretionary orogeny in the northern Tarim Craton. Tectonics 33, 302–329.

Ge, R., Zhu, W., Wilde, S.A., Wu, H., He, J., Zheng, B., 2014b. Archean magmatism and crustal evolution in the northern Tarim Craton: insights from zircon U-Pb-Hf-O isotopes and geochemistry of ~2.7 Ga orthogneiss and amphibolite in the Korla Complex. Precambr. Res. 252, 145–165.

Ge, R., Zhu, W., Wu, H., Zheng, B., He, J., 2013. Timing and mechanisms of multiple episodes of migmatization in the Korla Complex, northern Tarim Craton, NW China: Constraints from zircon U-Pb–Lu–Hf isotopes and implications for crustal growth. Precambr. Res. 231, 136–156.

Ge, R., Zhu, W., Zheng, B., Wu, H., He, J., Zhu, X., 2012. Early Pan-African magmatism in the Tarim Craton: insights from zircon U-Pb–Lu–Hf isotope and geochemistry of granitoids in the Korla area, NW China. Precambr. Res. 212, 117–138.

Glorie, S., De Grave, J., Buslov, M.M., Zhimulev, F.I., Stockli, D.F., Batalev, V.Y., Izmer, A., Van den Haute, P., Vanhaecke, F., Elburg, M.A., 2011. Tectonic history of the Kyrgyz South Tien Shan (Atbashi-Inylchek) suture zone: the role of inherited structures during deformation-propagation. Tectonics 30, C6016.

Green, T.H., 1995. Significance of Nb/Ta as an indicator of geochemical processes in the crust-mantle system. Chem. Geol. 120 (3–4), 347–359.

Han, C., Xiao, W., Su, B., Sakyi, P.A., Ao, S., Zhang, J., Wan, B., Song, D., Wang, Z., 2018. Ages and tectonic implications of the mafic–ultramafic-carbonatite intrusive rocks and associated Cu-Ni, Fe-P and apatite-vermiculite deposits from the Quruqtagh district, NW China. Ore Geol. Rev. 95, 1106–1122.

He, Z.Y., Klemd, R., Zhang, Z.M., Zong, K.Q., Sun, L.X., Tian, Z.L., Huang, B.T., 2015b. Mesoproterozoic continental arc magmatism and crustal growth in the eastern Central Tianshan Arc Terrane of the southern Central Asian Orogenic Belt: geochronological and geochemical evidence. Lithos 236–237, 74–89.

He, Z., Zhang, Z., Zong, K., Dong, X., 2013. Paleoproterozoic crustal evolution of the Tarim Craton: constrained by zircon U-Pb and Hf isotopes of meta-igneous rocks from Korla and Dunhuang. J. Asian Earth Sci. 78, 54–70.

He, Z., Klemd, R., Yan, L., Lu, T., Zhang, Z., 2018a. Mesoproterozoic juvenile crust in microcontinents of the Central Asian Orogenic Belt: evidence from oxygen and hafnium isotopes in zircon. Sci. Rep. 8 (1), 5054.

He, Z., Wang, B., Zhong, L., Zhu, X., 2018b. Crustal evolution of the Central Tianshan Block: insights from zircon U-Pb isotopic and structural data from meta-sedimentary and meta-igneous rocks along the Wulasitai-Wulanmoren shear zone. Precambr. Res. 314, 111–128.

He, J., Zhu, W., Zheng, B., Wu, H., Cui, X., Lu, Y., 2015a. Neoproterozoic diamictite-bearing sedimentary rocks in the northern Yili Block and their constraints on the Precambrian evolution of microcontinents in the Western Central Asian Orogenic Belt. Tectonophysics 665, 23–36.

Hoskin, P.W.O., Schaltegger, U., 2003. The composition of zircon and igneous and metamorphic petrogenesis. Rev. Mineral. Geochem. 53 (1), 27–55.

Hu, A., Jahn, B., Zhang, G., Chen, Y., Zhang, Q., 2000. Crustal evolution and Phanerozoic crustal growth in northern Xinjiang: Nd isotopic evidence. Part I. Isotopic characterization of basement rocks. Tectonophysics 328, 15–51.

Hu, Z., Liu, Y., Gao, S., Liu, W., Zhang, W., Tong, X., Lin, L., Zong, K., Li, M., Chen, H., Zhou, L., Liu, L., 2012. Improved in situ Hf isotope ratio analysis of zircon using newly designed X skimmer cone and jet sample cone in combination with the addition of nitrogen by laser ablation multiple collector ICP-MS. J. Anal. At. Spectrom. 27 (9), 1391–1399.

Hu, A.Q., Wei, G.J., Jahn, B.M., Zhang, J.B., Deng, W.F., Chen, L.L., 2010. Formation of the 0.9 Ga Neoproterozoic granitoids in the Tianshan Orogen, NW China: constraints from the SHRIMP zircon age determination and its tectonic significance. Geochimica 39, 197–212 (in Chinese with English abstract).

Huang, Z.Y., 2017. Precambrian Crustal Evolution of the Chinese Tianshan Belt. University of Chinese Academy of Sciences, Guangzhou (in Chinese with English abstract).

Huang, H., Cawood, P.A., Ni, S., Hou, M., Shi, Z., Hu, X., 2018. Provenance of late Paleozoic strata in the Yili Basin: implications for tectonic evolution of the South Tianshan orogenic belt. Geol. Soc. Am. Bull. 130 (5–6), 952–974.

Huang, H., Cawood, P.A., Hou, M., Xiong, F., Ni, S., Gong, T., 2019. Provenance of latest Mesoproterozoic to early Neoproterozoic (meta)-sedimentary rocks and implications for paleographic reconstruction of the Yili Block. Gondwana Res. 72, 120–138.

Huang, B., He, Z., Zong, K., Zhang, Z., 2014. Zircon U-Pb and Hf isotopic study of Neoproterozoic granitic gneisses from the Alatage area, Xinjiang: constraints on the Precambrian crustal evolution in the Central Tianshan Block. Chin. Sci. Bull. 59 (1), 100–112.

Huang, B.T., He, Z.Y., Zhang, Z.M., Klemd, R., Zong, K.Q., Zhao, Z.D., 2015a. Early Neoproterozoic granitic gneisses in the Chinese Eastern Tianshan: petrogenesis and tectonic implications. J. Asian Earth Sci. 113, 339–352.

Huang, Z., Long, X., Kröner, A., Yuan, C., Wang, Y., Chen, B., Zhang, Y., 2015b. Neoproterozoic granitic gneisses in the Chinese Central Tianshan Block: implications for tectonic affinity and Precambrian crustal evolution. Precambr. Res. 269, 73–89.

Huang, Z., Long, X., Yuan, C., Sun, M., Wang, Y., Zhang, Y., Chen, B., 2016. Detrital zircons from Neoproterozoic sedimentary rocks in the Yili Block: constraints on the affinity of microcontinents in the southern Central Asian Orogenic Belt. Gondwana Res. 37, 39–52.

Huang, Z., Long, X., Wang, X., Zhang, Y., Du, L., Yuan, C., Xiao, W., 2017. Precambrian evolution of the Chinese Central Tianshan Block: constraints on its tectonic affinity to the Tarim Craton and responses to supercontinental cycles. Precambr. Res. 295, 24–37.

Jackson, S.E., Pearson, N.J., Griffin, W.L., Belousova, E.A., 2004. The application of laser ablation-inductively coupled plasma-mass spectrometry to in situ U-Pb zircon geochronology. Chem. Geol. 211 (1–2), 47–69.

Kovach, V., Degtyarev, K., Tretyakov, A., Kotov, A., Tolmacheva, E., Wang, K.L., Chung, S.L., Lee, H.Y., Jahn, B.M., 2016. Sources and provenance of the Neoproterozoic placer deposits of the Northern Kazakhstan: implication for continental growth of the western Central Asian Orogenic Belt. Gondwana Res. 47, 28–43.

Kröner, A., Windley, B.F., Badarch, G., Tomurtogoo, O., Hegner, E., Jahn, B.M., Gruschka, S., Khain, E.V., Demoux, A., Wingate, M., 2007. Accretionary growth and crust formation in the Central Asian Orogenic Belt and comparison with the Arabian-Nubian shield. Geol. Soc. Am. Mem. 200, 181–209.

Kröner, A., Alexeiev, D.V., Hegner, E., Rojas-Agramonte, Y., Corsini, M., Chao, Y., Wong, J., Windley, B.F., Liu, D., Tretyakov, A.A., 2012. Zircon and muscovite ages, geochemistry, and Nd–Hf isotopes for the Aktyuz metamorphic terrane: Evidence for an Early Ordovician collisional belt in the northern Tianshan of Kyrgyzstan. Gondwana Res. 21, 901–927.

Kröner, A., Alexeiev, D.V., Rojas-Agramonte, Y., Hegner, E., Wong, J., Xia, X., Belousova, E., Mikolaichuk, A.V., Seltmann, R., Liu, D., 2013. Mesoproterozoic (Grenville-age) terranes in the Kyrgyz North Tianshan: zircon ages and Nd-Hf isotopic constraints on the origin and evolution of basement blocks in the southern Central Asian Orogen. Gondwana Res. 23, 272–295.

Kröner, A., Alexeiev, D.V., Kovach, V.P., Rojas-Agramonte, Y., Tretyakov, A.A., Mikolaichuk, A.V., Xie, H., Sobel, E.R., 2017. Zircon ages, geochemistry and Nd isotopic systematics for the Palaeoproterozoic 2.3 to 1.8 Ga Kuilyu Complex, East Kyrgyzstan – the oldest continental basement fragment in the Tianshan orogenic belt. J. Asian Earth Sci. 135, 122–135.

Lei, R., Wu, C., Chi, G., Gu, L., Dong, L., Qu, X., Jiang, Y., Jiang, S., 2013. The Neoproterozoic Hongliujing A-type granite in Central Tianshan (NW China): LA-ICP-MS zircon U-Pb geochronology, geochemistry, Nd-Hf isotope and tectonic significance. J. Asian Earth Sci. 74, 142–154.

Levashova, N.M., Meert, J.G., Gibsher, A.S., Grice, W.C., Bazhenov, M.L., 2011. The origin of microcontinents in the Central Asian Orogenic Belt: constraints from paleomagnetism and geochronology. Precambr. Res. 185, 37–54.

Li, Z.X., Bogdanova, S.V., Collins, A.S., Davidson, A., Waele, B.D., Ernst, R.E., Fitzsimons, I.C.W., Fuck, R.A., Gladkochub, D.P., Jacobs, J., 2008. Assembly, configuration, and break-up history of Rodinia: a synthesis. Precambr. Res. 160, 179–210.

Liou, J.G., Ernst, W.G., Song, S.G., Jahn, B.M., 2009. Tectonics and HP-UHP metamorphism of northern Tibet-Preface. J. Asian Earth Sci. 35, 191–198.

Liu, Y., Gao, S., Hu, Z., Gao, C., Zong, K., Wang, D., 2010. Continental and oceanic crust recycling-induced melt–peridotite interactions in the Trans-North China Orogen: U-Pb dating, Hf isotopes and trace elements in zircons from mantle xenoliths. J. Petrol. 51 (1–2), 537–571.

Liu, S.W., Guo, Z.J., Zhang, Z., Li, Q.G., Zheng, H.F., 2004. Nature of the Precambrian metamorphic blocks in the eastern segment of Central Tianshan: constraint from geochronology and Nd isotopic geochemistry. Sci. China, Ser. D Earth Sci. 47 (12), 1085–1094.

Liu, H., Wang, B., Shu, L., Jahn, B., Lizuka, Y., 2014. Detrital zircon ages of Proterozoic meta-sedimentary rocks and Paleozoic sedimentary cover of the northern Yili Block: implications for the tectonics of microcontinents in the Central Asian Orogenic Belt. Precambr. Res. 252, 209–222.

Liu, Y.S., Zong, K.Q., Kelemen, P.B., Gao, S., 2008. Geochemistry and magmatic history of eclogites and ultramafic rocks from the Chinese continental scientific drill hole: subduction and ultrahigh-pressure metamorphism of lower crustal cumulates. Chem. Geol. 247 (1–2), 133–153.

Long, L., Gao, J., Klemd, R., Beier, C., Qian, Q., Zhang, X., Wang, J., Jiang, T., 2011. Geochemical and geochronological studies of granitoid rocks from the Western Tianshan Orogen: implications for continental growth in the southwestern Central Asian Orogenic Belt. Lithos 126, 321–340.

Lu, S., Li, H., Zhang, C., Niu, G., 2008. Geological and geochronological evidence for the Precambrian evolution of the Tarim Craton and surrounding continental fragments. Precambr. Res. 160, 94–107.

Ludwig, K.R., 2003. In: User's Manual for Isoplot/Ex Version 3.00: A Geochronological Toolkit for Microsoft Excel. Berkeley Geochronology Center, Special Publication, California, Berkeley, pp. 39.

Ma, Y.J., Liu, C.Q., 2001. Sr isotope evolution during chemical weathering of granites. Sci. China, Ser. D Earth Sci. 44 (8), 726–734.

Ma, Q., Zheng, J., Griffin, W.L., Zhang, M., Tang, H., Su, Y., Ping, X., 2012. Triassic "adakitic" rocks in an extensional setting (North China): melts from the cratonic lower crust. Lithos 149, 159–173.

Maniar, P.D., Piccoli, P.M., 1989. Tectonic discrimination of granitoids. Geol. Soc. Am. Bull. 101 (5), 635–643.

Middlemost, E.A.K., 1994. Naming materials in the magma/igneous rock system. Earth Sci. Rev. 37 (3–4), 215–224.

Morales Cámera, M.M., Dahlquist, J.A., Basei, M.A.S., Galindo, C., Da Costa Campos Neto, M., Facetti, N., 2017. F-rich strongly peraluminous A-type magmatism in the pre-Andean foreland Sierras Pampeanas, Argentina: Geochemical, geochronological, isotopic constraints and petrogenesis. Lithos 277, 210–227.

Morel, M.L.A., Nebel, O., Nebel-Jacobsen, Y.J., Miller, J.S., Vroon, P.Z., 2008. Hafnium isotope characterization of the GJ-1 zircon reference material by solution and laser-ablation MC-ICPMS. Chem. Geol. 255 (1–2), 231–235.

Patiño Douce, A.E., Beard, J.S., 1996. Effects of P, f(O_2) and Mg/Fe ratio on dehydration melting of model metagreywackes. J. Petrol. 37 (5), 999–1024.

Patiño Douce, A.E., Johnston, A.D., 1991. Phase equilibria and melt productivity in the pelitic system: implications for the origin of peraluminous granitoids and aluminous granulites. Contrib. Miner. Petrol. 107 (2), 202–218.

Pearce, J.A., 1996. Sources and settings of granitic rocks. Episodes 19, 120–125.

Pearce, J.A., Harris, N., Tindle, A.G., 1984. Trace element discrimination diagrams for the tectonic interpretation of granitic rocks. J. Petrol. 25 (4), 956–983.

Pilitsyna, A.V., Tretyakov, A.A., Degtyarev, K.E., Salnikova, E.B., Kotov, A.B., Kovach, V.P., Wang, K.L., Batanova, V.G., Plotkina, Y.V., Tolmacheva, E.V., Ermolaev, B.V., 2019. Early Palaeozoic metamorphism of Precambrian crust in the Zheltau terrane (Southern Kazakhstan; Central Asian Orogenic belt): P-T paths, protoliths, zircon dating and tectonic implications. Lithos 324, 115–140.

Qian, Q., Gao, J., Klemd, R., He, G., Song, B., Liu, D., Xu, R., 2009. Early Paleozoic tectonic evolution of the Chinese South Tianshan Orogen: constraints from SHRIMP zircon U-Pb geochronology and geochemistry of basaltic and dioritic rocks from Xiate, NW China. Int. J. Earth Sci. 98 (3), 551–569.

Rapp, R.P., Watson, E.B., 1995. Dehydration melting of metabasalt at 8–32 kbar: Implications for continental growth and crust-mantle recycling. J. Petrol. 36 (4), 891–931.

Stern, C.R., Kilian, R., 1996. Role of the subducted slab, mantle wedge and continental crust in the generation of adakites from the Andean Austral Volcanic Zone. Contrib. Miner. Petrol. 123 (3), 263–281.

Sun, S.S., McDonough, W.F., 1989. Chemical and isotopic systematics of oceanic basalts: implications for mantle composition and processes. Geol. Soc., London, Spec. Publ. 42, 313–345.

Sylvester, P.J., 1989. Post-collisional alkaline granites. J. Geol. 97 (3), 261–280.

Tanaka, T., Togashi, S., Kamioka, H., Amakawa, H., Kagami, H., Hamamoto, T., Yuhara, M., Orihashi, Y., Yoneda, S., Shimizu, H., Kunimaru, T., Takahashi, K., Yanagi, T., Nakano, T., Fujimaki, H., Shinjo, R., Asahara, Y., Tanimizu, M., Dragusanu, C., 2000. JNdi-1: a neodymium isotopic reference in consistency with LaJolla neodymium. Chem. Geol. 168 (3–4), 279–281.

Tang, Q., Zhang, Z., Li, C., Wang, Y., Ripley, E.M., 2016. Neoproterozoic subduction-related basaltic magmatism in the northern margin of the Tarim Craton: implications for Rodinia reconstruction. Precambr. Res. 286, 370–378.

Taylor, S.R., McLennan, S.M., 1985. The Continental Crust: Its Composition and Evolution. Blackwell Scientific Publications, Oxford, pp. 312.

Thirlwall, M.F., 1991. Long-term reproducibility of multicollector Sr and Nd isotope ratio analysis. Chem. Geol. 94 (2), 85–104.

Tretyakov, A.A., Degtyarev, K.E., Salnikova, E.B., Shatagin, K.N., Letnikova, E.F., Anisimova, I.V., Yakovleva, S.Z., 2011. Late Precambrian magmatism of southern Ulutau (central Kazakhstan). In: Sklyarov, E.V. (Ed.), Geodynamic Evolution of Lithosphere of the Central Asian Active Belt (From Ocean to Continent): Materials of Conference. Issue 9. Institute of Earth's Crust, Irkutsk, pp. 213–215.

Tretyakov, A.A., Degtyarev, K.E., Salnikova, E.B., Shatagin, K.N., Kotov, A.B., Anisimova, I.V., Plotkina, Y.V., 2017. The late Tonian Zhaunkar granite complex of the Ulutau sialic massif, Central Kazakhstan. Dokl. Earth Sci. 473, 411–415.

Tretyakov, A.A., Degtyarev, K.E., Shatagin, K.N., Kotov, A.B., Sal Nikova, E.B., Anisimova, I.V., 2015. Neoproterozoic anorogenic rhyolite-granite volcanoplutonic association of the Aktau-Mointy sialic massif (Central Kazakhstan): age, source, and paleotectonic position. Petrology 23, 22–44.

Vielzeuf, D., Holloway, J.R., 1988. Experimental determination of the fluid-absent melting relations in the pelitic system. Contrib. Miner. Petrol. 98 (3), 257–276.

Wang, X., Gao, J., Klemd, R., Jiang, T., Li, J., Zhang, X., Tan, Z., Li, L., Zhu, Z., 2014c. Geochemistry and geochronology of the Precambrian high-grade metamorphic complex in the Southern Central Tianshan ophiolitic mélange, NW China. Precambr. Res. 254, 129–148.

Wang, X., Gao, J., Klemd, R., Jiang, T., Li, J., Zhang, X., Xue, S., 2017. The Central Tianshan Block: a microcontinent with a Neoarchean-Paleoproterozoic basement in the southwestern Central Asian Orogenic Belt. Precambr. Res. 295, 130–150.

Wang, Z.M., Han, C.M., Xiao, W.J., Su, B.X., Sakyi, P.A., Song, D.F., Lin, L.N., 2014d. The petrogenesis and tectonic implications of the granitoid gneisses from Xingxingxia in the eastern segment of Central Tianshan. J. Asian Earth Sci. 88, 277–292.

Wang, Y.X., Li, H.M., Tao, X.C., Yang, H., Gu, L.X., Guo, J.C., 1991. A study of Nd, Sr and O isotopes and the crustal growth age of granites in Eastern segment of middle East Tianshan Belt, China. Acta Petrol. Sin. 3, 19–26 (in Chinese with English abstract).

Wang, B., Liu, H., Shu, L., Jahn, B., Chung, S., Zhai, Y., Liu, D., 2014a. Early Neoproterozoic crustal evolution in northern Yili Block: insights from migmatite, orthogneiss and leucogranite of the Wenquan metamorphic complex in the NW Chinese Tianshan. Precambr. Res. 242, 58–81.

Wang, C., Liu, L., Wang, Y., He, S., Li, R., Li, M., Yang, W., Cao, Y., Collins, A.S., Shi, C., 2015a. Recognition and tectonic implications of an extensive Neoproterozoic volcano-sedimentary rift basin along the southwestern margin of the Tarim Craton, northwestern China. Precambr. Res. 257, 65–82.

Wang, B., Shu, L., Liu, H., Gong, H., Ma, Y., Mu, L., Zhong, L., 2014b. First evidence for ca. 780 Ma intra-plate magmatism and its implications for Neoproterozoic rifting of the North Yili Block and tectonic origin of the continental blocks in SW of Central Asia. Precambr. Res. 254, 258–272.

Wang, C., Zhang, J., Li, M., Li, R., Peng, Y., 2015b. Generation of ca. 900–870 Ma bimodal rifting volcanism along the southwestern margin of the Tarim Craton and its implications for the Tarim–north China connection in the early Neoproterozoic. J. Asian Earth Sci. 113, 610–625.

Whalen, J.B., Currie, K.L., Chappell, B.W., 1987. A-type granites: geochemical characteristics, discrimination and petrogenesis. Contrib. Miner. Petrol. 95 (4), 407–419.

Wiedenbeck, M., Alle, P., Corfu, F., Griffin, W.L., Meier, M., Oberli, F., Quadt, A., Roddick, J.C., Spiegel, W., 1995. Three natural zircon standards for U-Th-Pb, Lu-Hf trace element and REE analyses. Geostand. Geoanal. Res. 19 (1), 1–23.

Wu, F., Liu, X., Ji, W., Wang, J., Yang, L., 2017. Highly fractionated granites: recognition and research. Sci. China Earth Sci. 60 (7), 1201–1219.

Wu, C.Z., Santosh, M., Chen, Y.J., Samson, I.M., Lei, R.X., Dong, L.H., Qu, X., Gu, L.X., 2014. Geochronology and geochemistry of Early Mesoproterozoic meta-diabase sills from Quruqtagh in the northeastern Tarim Craton: implications for breakup of the Columbia supercontinent. Precambr. Res. 241, 29–43.

Wu, G., Xiao, Y., Bonin, B., Ma, D., Li, X., Zhu, G., 2018. Ca. 850 Ma magmatic events in the Tarim Craton: age, geochemistry and implications for assembly of Rodinia supercontinent. Precambr. Res. 305, 489–503.

XBGMR (Xinjiang Bureau of Geology and Mineral Resources), 1993. Regional Geology of Xinjiang Uygur Autonomy Region. Geology Publishing House, Beijing, pp. 1–841.

XBGMR (Xinjiang Bureau of Geology and Mineral Resources), 1978. Regional Report of the Mohe'er Area at scale of 1: 50 000 (unpublished).

Xu, Z., He, B., Zhang, C., Zhang, J., Wang, Z., Cai, Z., 2013. Tectonic framework and crustal evolution of the Precambrian basement of the Tarim Block in NW China: new geochronological evidence from deep drilling samples. Precambr. Res. 235, 150–162.

Yang, T.N., Li, J.Y., Sun, G.H., Wang, Y.B., 2008. Mesoproterozoic continental arc type granite in the Central Tianshan mountains: zircon SHRIMP U-Pb dating and geochemical analyses. Acta Geol. Sin.-English Ed. 82 (1), 117–125.

Yang, H., Wu, G., Kusky, T.M., Chen, Y., Xiao, Y., 2018. Paleoproterozoic assembly of the North and South Tarim terranes: new insights from deep seismic profiles and Precambrian granite cores. Precambr. Res. 305, 151–165.

Ye, H.M., Li, X.H., Lan, Z.W., 2013. Geochemical and Sr-Nd-Hf-O-C isotopic constraints on the origin of the Neoproterozoic Qieganbulake ultramafic-carbonatite complex from the Tarim Block, Northwest China. Lithos 182, 150–164.

Ye, X., Zhang, C., Santosh, M., Zhang, J., Fan, X., Zhang, J., 2016. Growth and evolution of Precambrian continental crust in the southwestern Tarim terrane: new evidence from the ca. 1.4 Ga A-type granites and Paleoproterozoic intrusive complex. Precambr. Res. 275, 18–34.

Zhang, Z., Kang, J., Kusky, T., Santosh, M., Huang, H., Zhang, D., Zhu, J., 2012c. Geochronology, geochemistry and petrogenesis of Neoproterozoic basalts from Sugetbrak, northwest Tarim block, China: implications for the onset of Rodinia supercontinent breakup. Precambr. Res. 220–221, 158–176.

Zhang, C., Li, X., Li, Z., Lu, S., Ye, H., Li, H., 2007a. Neoproterozoic ultramafic–mafic-carbonatite complex and granitoids in Quruqtagh of northeastern Tarim Block, western China: geochronology, geochemistry and tectonic implications. Precambr. Res. 152, 149–169.

Zhang, C., Li, Z., Li, X., Yu, H., Ye, H., 2007b. An early Paleoproterozoic high-K intrusive complex in southwestern Tarim Block, NW China: age, geochemistry, and tectonic implications. Gondwana Res. 12, 101–112.

Zhang, C., Li, Z., Li, X., Ye, H., 2009. Neoproterozoic mafic dyke swarms at the northern margin of the Tarim Block, NW China: age, geochemistry, petrogenesis and tectonic implications. J. Asian Earth Sci. 35, 167–179.

Zhang, C., Yang, D., Wang, H., Takahashi, Y., Ye, H., 2011. Neoproterozoic mafic-ultramafic layered intrusion in Quruqtagh of northeastern Tarim Block, NW China: two phases of mafic igneous activity with different mantle sources. Gondwana Res. 19, 177–190.

Zhang, C., Li, H., Santosh, M., Li, Z., Zou, H., Wang, H., Ye, H., 2012a. Precambrian evolution and cratonization of the Tarim Block, NW China: petrology, geochemistry, Nd-isotopes and U-Pb zircon geochronology from Archaean gabbro-TTG-potassic granite suite and Paleoproterozoic metamorphic belt. J. Asian Earth Sci. 47, 5–20.

Zhang, W.R., Zhu, W.G., Wang, S.X., 2006. The Meso-Neoproterozoic carbonate environment of Kekesu River area in western Tianshan. Gansu Geol. 15, 25–28 (in Chinese with English Abstract).

Zhang, C., Zou, H., Wang, H., Li, H., Ye, H., 2012b. Multiple phases of the Neoproterozoic igneous activity in Quruqtagh of the northeastern Tarim Block, NW China: interaction between plate subduction and mantle plume? Precambr. Res. 222–223, 488–502.

Zhang, C., Zou, H., Li, H., Wang, H., 2013. Tectonic framework and evolution of the Tarim Block in NW China. Gondwana Res. 23, 1306–1315.

Zhou, J.B., Wilde, S.A., Zhao, G.C., Han, J., 2018. Nature and assembly of microcontinental blocks within the Paleo-Asian Ocean. Earth Sci. Rev. 186, 76–93.

Zong, K., Liu, Y., Zhang, Z., He, Z., Hu, Z., Guo, J., Chen, K., 2013. The generation and evolution of Archean continental crust in the Dunhuang block, northeastern Tarim craton, northwestern China. Precambr. Res. 235, 251–263.

Zong, K., Klemd, R., Yuan, Y., He, Z., Guo, J., Shi, X., Liu, Y., Hu, Z., Zhang, Z., 2017. The assembly of Rodinia: the correlation of early Neoproterozoic (ca. 900 Ma) high-grade metamorphism and continental arc formation in the southern Beishan Orogen, southern Central Asian Orogenic Belt (CAOB). Precambr. Res. 290, 32–48.